Research Square

Preprints are preliminary reports that have not undergone peer review.
They should not be considered conclusive, used to inform clinical practice,
or referenced by the media as validated information.

ZIP13/SLC39A13 integrates intracellular iron distribution with adipose energy metabolism

Toshiyuki Fukada

fukada@ph.bunri-u.ac.jp

Tokushima Bunri University

Ayako Fukunaka

Institute for Molecular & Cellular Regulation, Gunma University

Gen Tanaka

Kyorin University

Toru Kimura

Josai University

Kowit Hengphasatporn

University of Tsukuba

Daisuke Saito

Institute for Molecular & Cellular Regulation, Gunma University

Mayo Shigeta

RIKEN Center for Biosystems Dynamics Research

Hiroshi Shibata

Laboratory of Epigenetics and Metabolism, Institute for Molecular and Cellular Regulation, Gunma University, Gunma 371-8512, Japan

Takayuki Ichinose

Toray Research Center, Inc.,

Ichitaro Abe

The University of Tokyo https://orcid.org/0000-0002-2769-5338

Mari Shimura

National Center for Global Health and Medicine https://orcid.org/0000-0002-8406-6327

Takashi Sato

Gumma University

Yuko Nakagawa

IMCR, Gunma University

Takuro Horii

Gunma University https://orcid.org/0009-0004-2167-1791

Izuho Hatada

Gunma University https://orcid.org/0000-0001-7225-3929

Shingo Kajimura
Beth Israel Deaconess Medical Center, Harvard Medical School, and Howard Hughes Medical Institute
https://orcid.org/0000-0003-0672-5910
Hiroshi Kiyonari
RIKEN Center for Biosystems Dynamics Research https://orcid.org/0000-0002-1509-8747
Hiroyuki Sakurai
Kyorin University School of Medicine
Yasuteru Shigeta
University of Tsukuba https://orcid.org/0000-0002-3219-6007
Hirotaka Watada
Juntendo University https://orcid.org/0000-0001-5961-1816
Yoshio Fujitani
Institute for Molecular & Cellular Regulation, Gunma University

---

Article

Keywords: zinc, iron, transporter, organelle, adipocyte, lipid metabolism, ZIP13/SLC39A13

Posted Date: June 2nd, 2026

DOI: https://doi.org/10.21203/rs.3.rs-3991001/v1

License: This work is licensed under a Creative Commons Attribution 4.0 International License.
Read Full License

Additional Declarations: There is **NO** Competing Interest.

ZIP13/SLC39A13 integrates intracellular iron distribution with adipose energy metabolism

Ayako Fukunaka[1#*], Gen Tanaka[2#], Toru Kimura[2,3#], Kowit Hengphasatporn[4], Daisuke Saito[1,5], Mayo Shigeta[6], Hiroshi Shibata[7], Takayuki Ichinose[8], Ichitaro Abe[9,10,11], Mari Shimura[12,13], Takashi Sato[1], Yuko Nakagawa[1], Takuro Horii[14], Izuho Hatada[14,15], Shingo Kajimura[10], Hiroshi Kiyonari[6], Hiroyuki Sakurai[2], Yasuteru Shigeta[4], Hirotaka Watada[5], Toshiyuki Fukada[16*], and Yoshio Fujitani[1*]

[1] Laboratory of Developmental Biology & Metabolism, Institute for Molecular & Cellular Regulation, Gunma University, Gunma, Japan

[2] Department of Pharmacology and Toxicology, Kyorin University School of Medicine, Tokyo, Japan

[3] Laboratory of Biomedicinal Science, Department of Pharmaceutical Science, Faculty of Pharmacy and Pharmaceutical Science, Josai University, Saitama, Japan

[4] Center for Computational Sciences, University of Tsukuba, Ibaraki, Japan

[5] Department of Metabolism & Endocrinology, Juntendo University Graduate School of Medicine, Tokyo, Japan

[6] Laboratory for Animal Resources and Genetic Engineering, RIKEN Center for Biosystems Dynamics Research, Hyogo, Japan

[7] Laboratory of Epigenetics and Metabolism, Institute for Molecular & Cellular Regulation, Gunma University, Gunma, Japan

[8] Inorganic Analysis Laboratories, Toray Research Center, Inc., Shiga, Japan

[9] Department of Cardiology and Clinical Examination, Faculty of Medicine, Oita University, Oita, Japan

[10] Division of Endocrinology, Diabetes and Metabolism, Beth Israel Deaconess Medical Center and Harvard Medical School, Boston, MA, USA

[11] Department of Frontier Cardiovascular Science, Graduate School of Medicine, The University of Tokyo, Tokyo, Japan

[12] National Institute of Global Health and Medicine, Japan Institute for Health Security, Tokyo, Japan

[13] RIKEN SPring-8 Center, Hyogo, Japan

[14] Laboratory of Genome Science, Institute for Molecular & Cellular Regulation, Gunma University, Gunma, Japan

[15] Viral Vector Core, Gunma University Initiative for Advanced Research, Gunma, Japan

[16] Laboratory of Molecular and Cellular Physiology, Faculty of Pharmaceutical Sciences, Tokushima Bunri University, Tokushima, Japan

***Corresponding authors**

E-mail: fukada@ph-bunri-u.ac.jp (T.F.), fukunaka@gunma-u.ac.jp (A.F.), and fujitani@gunma-u.ac.jp (Y.F.)

[#] These authors contributed equally to this work.

***Keywords*:** zinc, iron, transporter, organelle, adipocyte, lipid metabolism, ZIP13/SLC39A13

***Running title*:** ZIP13-mediated iron regulates lipolysis and thermogenesis

Abbreviations:

RER: respiratory exchange ratio, HFD: high-fat diet, STD: standard diet, ER, endoplasmic reticulum, PKA: protein kinase A, cAMP: cyclic AMP, ICP-MS: inductively coupled plasma mass spectrometry, EDSSPD3: Ehlers-Danlos syndrome spondylocheirodysplastic type 3, NEFA: nonesterified fatty acid, MT: metallothionein, PDE: phosphodiesterase, 4F2hc: 4F2 cell-surface antigen heavy chain, SVF: stromal vascular fraction, IRP2: iron regulatory protein 2, TfR: transferrin receptor, Fth1: ferritin heavy chain, FTL: ferritin light chain, NAC: N-acetylcysteine, WAT: white adipose tissue, aP2: adipocyte Protein 2, HSL: hormone-sensitive lipase, CREB: cyclic adenosine monophosphate-responsive element-binding protein, ROS: reactive oxygen species, BAT: brown adipose tissue, Ctrl: control, UCP1: Uncoupling protein 1

Abstract

Fine-tuning of lipid metabolism in adipose tissue is crucial for maintaining energy homeostasis and metabolic health. Beyond total metal abundance, the intracellular distribution of metal ions represents a fundamental yet largely unexplored regulatory layer of cellular metabolism. Here, we demonstrate that ZIP13/SLC39A13, originally identified as an intracellular zinc transporter, regulates the subcellular distribution of iron. This function limits iron-dependent reactive oxygen species production, thereby restraining excessive cAMP/PKA signaling in mature adipocytes. Consequently, ZIP13 suppresses β-adrenergic receptor-stimulated lipolysis in subcutaneous white adipose tissue, as well as thermogenesis in brown adipose tissue. Notably, ZIP13 exhibits a context-dependent shift in substrate utilization during adipocyte differentiation, transitioning from zinc transport in preadipocytes to iron transport in mature adipocytes. In humans, ZIP13 mutations cause spondylocheirodysplastic Ehlers-Danlos syndrome with lipoatrophy, supporting the physiological relevance of intracellular metal distribution in metabolic regulation. Together, these findings establish intracellular metal distribution—rather than total metal abundance—as a fundamental principle governing cellular metabolism.

Introduction

Precise regulation of lipid metabolism in adipose tissue is essential for maintaining energy balance and metabolic health. Adipose tissue, a key regulator of energy homeostasis, is composed of white and brown adipocytes, which have two distinct functions; i.e., white adipocytes store excess energy, whereas brown adipocytes are specialized for energy consumption (1, 2). The thermogenic adipocytes, including both brown and beige adipocytes, are associated with improved systemic metabolic health, such as enhanced insulin sensitivity and glucose homeostasis. In contrast, the activity of thermogenic adipocytes declines with age and in obesity in both mice and humans (3). Although chronic caloric excess is widely recognized as a major cause of diabetes and obesity-related diseases, previous research has focused almost exclusively on macronutrients. As a result, the potential roles of micronutrients, especially trace metals and their regulatory proteins, have historically received less attention, but are now increasingly recognized as critical regulators of metabolic processes (4, 5, 6, 7). Importantly, beyond total abundance, the intracellular distribution of metal ions represents a critical but poorly understood regulatory layer of cellular metabolism.

Metal ion concentrations within cellular compartments are integrally regulated by transporters localized at the plasma membrane and within intracellular compartments. Maintaining appropriate metal ion levels within cells is crucial for cellular function. For example, zinc is essential for insulin secretion and action, and its dysregulation is linked to diabetes and obesity-associated diseases (8). Ferrous iron (Fe^{2+}) can generate reactive oxygen species (ROS), which, if unregulated, damage lipids,

proteins, and DNA (9, 10), thereby contributing to metabolic disorders, such as insulin resistance and obesity-associated inflammation (11, 12). Although these metal ions are involved in diverse adipocyte functions (13, 14), it remains unclear how imbalances in their intracellular distribution affect adipocyte functions and associated metabolic diseases.

Divalent metal ions are transported by members of the Zrt/Irt proteins (ZIP/SLC39A) family (15). While ZIP transporters are initially characterized as zinc importers, some members, including ZIP8 and ZIP14, exhibit broader substrate specificity and transport multiple divalent metal ions, such as zinc, iron, and manganese (16, 17, 18, 19, 20). Although many ZIP proteins localize to the plasma membrane, some members are found in intracellular compartments, including the endoplasmic reticulum (ER) and Golgi apparatus (21, 22). ZIP13, in particular, is localized to the Golgi apparatus, which suggests that it plays a role in regulating subcellular metal distribution. Previous studies have implicated ZIP13 in zinc homeostasis and adipose tissue function; dysfunction of this gene causes Ehlers-Danlos syndrome spondylocheirodysplastic type 3 (EDSSPD3, OMIM 612350), an autosomal-recessive disorder in humans characterized by lipoatrophy, and leads to alteration in beige adipocyte differentiation and energy expenditure in mice (23, 24, 25, 26). However, it remains unclear whether these phenotypes can be explained by impaired zinc transport alone, raising the possibility that additional metal substrates and mechanisms are involved. Furthermore, the extent to which adipose phenotypes associated with ZIP13 dysfunction are driven by enhanced beige adipocyte differentiation remains to be determined.

In this study, we demonstrate that ZIP13 dynamically switches its primary transport substrate from Zn^{2+} to Fe^{2+} during adipocyte maturation, and that ZIP13-mediated intracellular iron distribution is essential for proper lipid metabolism in adipocytes. These findings reveal a differentiation-dependent mechanism of metal transport and establish intracellular metal distribution—rather than total metal abundance—as a fundamental regulatory principle of adipose tissue metabolism.

Results

Adipo-*Zip13*KO mice demonstrate accelerated lipolysis and thermogenesis

To clarify the intrinsic role of ZIP13 in mature adipocytes, we generated adipocyte-specific *Zip13* knockout mice (Adipo-*Zip13*KO) by crossing *Zip13*$^{flox/-}$ mice with *Adiponectin*-Cre mice to increase knockout efficiency as previously applied in other various studies (27, 28). We confirmed that *Zip13* mRNA expression was significantly reduced in all fat tissues analyzed (Fig. 1A). Under standard diet (STD) conditions, metabolic parameters, including oxygen consumption (VO_2) (Fig. S1A, B), food intake (Fig. S1C), locomotor activity (Fig. S1D), and rectal temperature (Fig. S1E), were comparable between Adipo-*Zip13*KO and control (Ctrl) mice. Additionally, gene expression profiling, histological analysis, and VO_2 measurement at different environmental temperatures revealed no obvious change regarding the beige adipocyte biogenesis in the subcutaneous fat tissue of Adipo-*Zip13*KO mice (Fig. S1F-S1I).

On the other hand, respiratory exchange ratio (RER) was significantly lower in Adipo-*Zip13*KO mice, similar to the phenotype observed in systemic *Zip13*KO mice (23) (Fig. 1B-C and Fig. S2A-B), suggesting that these mice preferentially utilize lipids as an energy source rather than carbohydrates. To investigate the cause of the decreased RER, we hypothesized that lipolysis might be enhanced in *Zip13*-KO mature adipocytes. To test this, we measured plasma levels of circulating non-esterified fatty acids (NEFAs) in response to the β3-adrenergic receptor agonist CL316,243, which stimulates sympathetic nerve-mediated lipolysis. In the basal state, plasma NEFA levels were

modestly increased in male Adipo-*Zip13*KO mice compared with male Ctrl mice (Fig. 1D), and this was also observed in female mice (Fig. S2C), indicating enhanced lipolysis under resting conditions. Upon CL316,243 stimulation, both groups reached similar maximal NEFA levels (Fig. 1D), suggesting that the lipolytic response was saturated and obscured genotype-dependent differences. We also identified subcutaneous fat as the major contributor to this increase NEFA release under the stimulation of β-adrenergic receptor agonist isoproterenol (Fig. 1E and S2D). To determine whether this enhanced lipolysis occurs in a cell-autonomous manner, we isolated preadipocytes from the subcutaneous fat tissue of Ctrl and Adipo-*Zip13*KO mice and differentiated them into white adipocytes. Despite similar differentiation efficiency (Fig. S2E), NEFA release in response to isoproterenol was significantly elevated in *Zip13*-deficient adipocytes (Fig. 1F). Gene expression of lipolysis- and lipid metabolism- related markers in subcutaneous fat did not differ between Adipo-*Zip13*KO mice and Ctrl mice (Fig. S2F), suggesting that enhanced β-adrenergic signaling in *Zip13*-deficienct adipocytes occurs without notable changes in the expression genes involved in lipolysis.

Given that *Zip13* expression is upregulated under high-fat diet (HFD) conditions (Fig. 2A), we next evaluated body weight under STD and HFD. Adipo-*Zip13*KO mice appeared to be resistant to HFD-induce weight gain (Fig. 2B), similar to systemic *Zip13*-KO mice (23). Adipo-*Zip13*KO mice aged 30 weeks or older exhibited lower body weight than Ctrl mice, even when fed a standard diet (STD) (Fig. 2C), along with decreased fat mass, particularly in subcutaneous depots (Fig. 2D, S3A and S3B). Although glucose tolerance was normal, insulin level was lower in Adipo-*Zip13*KO mice

compared to Ctrl mice under STD conditions (Fig. S3C and D). Correspondingly, these mice showed improved insulin sensitivity under HFD conditions (Fig. S3E). Taken together, these results indicate that Adipo-*Zip13*KO mice are less prone to HFD-induced obesity and insulin resistance.

As increased lipolysis alone does not usually lead to weight loss, we hypothesized that increased thermogenesis in brown adipose tissue (BAT) might be involved in the lean phenotype. To test this, we measured the rectal temperature of mice in response to cold exposure, and observed significantly higher temperatures in Adipo-*Zip13*KO mice (Fig. S3F) than in Ctrl mice, suggesting that either muscle shivering thermogenesis or BAT-mediated non-shivering thermogenesis may be enhanced. We next assessed VO_2 under thermoneutral conditions (30 °C) following stimulation with CL316,243. VO_2 was significantly increased in Adipo-*Zip13*KO mice compared to Ctrl mice after CL316,243 treatment (Fig. 2E), which was also observed in female mice (Fig. S3G), suggesting that ZIP13 may regulate thermogenic responses. Collectively, these findings suggest that a modest but significant increase in whole-body oxygen consumption contributes to resistance to HFD-induced obesity and protection against insulin resistance in Adipo-*Zip13*KO mice.

Upregulation of cytosolic iron levels in mature adipocytes from Adipo-*Zip13*KO mice

Since ZIP13 belongs to the ZIP family, which transports divalent metals (29), we next measured cellular zinc and iron levels using inductively coupled plasma mass spectrometry (ICP-MS), showing that total zinc and iron levels analyzed by ICP-MS in whole cells were comparable

between Ctrl and Adipo-*Zip13*KO mature adipocytes (Fig. 3A). ZIP13 localizes to both the ER and Golgi (Fig. 3B), so we examined the subcellular distribution of zinc and iron ions by using chemical probes (FluoZin-3 and FerroOrange (30) (Fig. S4A) for zinc ions (Zn^{2+}) and the ferrous iron ions (Fe^{2+}), respectively), and found that ER and Golgi-associated Fe^{2+} levels were decreased in mature *Zip13*-KO adipocytes, whereas Zn^{2+} levels were not changed (Fig. 3C). Intracellular iron homeostasis is primarily regulated through the post-transcriptional control of iron metabolism genes, including ferritin heavy chain (Fth1), ferritin light chain (FTL), and transferrin receptor (TfR), via the iron responsive element-iron regulatory protein (IRE-IRP) system (10). We analyzed the expression of iron metabolism-associated proteins, IRP2, TfR, Fth1, and FTL, and found that their expression tended to be changed in the basal condition in Adipo-*Zip13*KO cells, which became more substantial upon stimulation with isoproterenol (Fig. 3D, E, and F). Although changes in protein expression do not directly demonstrate alteration in Fe^{2+} concentration, these results are consistent with a redistribution of Fe^{2+} from ER/Golgi to the cytosol in *Zip13*-KO mature adipocytes. Importantly, total cellular iron levels were unchanged, whereas its subcellular distribution was markedly altered, indicating that intracellular Fe^{2+} localization, rather than total abundance, is a key determinant of adipocyte metabolic regulation. Furthermore, the mechanism by which *Zip13*-KO adipocytes still take up Zn^{2+} can be explained by the fact that some ZIP family members, including ZIP7, ZIP9, and ZIP11, which are also localized to the ER/Golgi, may compensate for the absence of ZIP13 in *Zip13*-KO adipocytes. This redundancy likely accounts for the unchanged Zn^{2+} levels in Adipo-*Zip13*KO

cells, whereas Fe^{2+} distribution is altered in a compartment-dependent manner.

ZIP13 negatively regulates lipolysis and thermogenesis through Fe^{2+} transport

The above results suggested that ZIP13-mediated Fe^{2+} homeostasis leads to the negative regulation of lipolysis in mature adipocytes. This was reminiscent of a previous study showing that iron-mediated lipolysis is caused by a pro-oxidant mechanism, in which supplementation with the antioxidant N-acetyl cysteine (NAC) was shown to cancel iron-induced NEFA release (31). Therefore, we tested whether NAC treatment can affect lipolysis in *Zip13*-KO mature adipocytes, and found that NAC treatment restores the accelerated NEFA release in *Zip13*-KO mature adipocytes (Fig. 4A). Furthermore, hydroxyl radicals, which are one of the products of the Fe^{2+}-mediated Fenton reaction, was increased in Adipo-*Zip13*KO cells (Fig. S4B), indicating that dysfunction of ZIP13 may increases cytoplasmic Fe^{2+} and pro-oxidants levels, leading to the enhancement of NEFA release.

We next examined the activation status of the cAMP/PKA signaling pathway, a key mediator of β-adrenergic receptor-stimulated lipolysis (32). The levels of cAMP, phosphorylated PKA (pPKA), and downstream targets of PKA were increased in *Zip13*-KO mature adipocytes (Fig. 4B-C, and Fig. S4C). NEFA release from *Zip13*-KO mature adipocytes was increased even upon treatment with forskolin (Fig. 4D), suggesting that the cAMP degradation system would be disturbed in *Zip13*-KO mature adipocytes. Consistent with this, the activity of PDE, the primary enzyme responsible for degrading intracellular cAMP, was decreased in *Zip13*-KO mature adipocytes (Fig. 4E). Inhibition of

PDE3 increased NEFA release from Ctrl differentiated adipocytes and primary mature adipocytes but not from *Zip13*-KO adipocytes, whereas inhibition of PDE4 did not lead to a similar increase in NEFA release (Fig. S5A and B). As PDE3B is predominantly expressed in adipocytes (13), we knocked down *Pde3b* in mature adipocytes by small interfering RNA (siRNA), and found that NEFA release is upregulated in *Pde3b*-repressed Ctrl cells, whereas such changes were not observed in *Pde3b*-repressed Adipo-*Zip13*KO cells (Fig. S5C and D). These results suggest that *Zip13* deficiency likely contributing to impaired PDE3B activity in mature adipocytes, which may be responsible for the increased cAMP levels leading to the acceleration of lipolysis.

We noted that under basal conditions, cytosolic Fe^{2+} levels already showed a tendency to increase in Adipo-*Zip13*KO cells (Fig.3D-F), and PDE activity was inhibited in these cells (Fig.4E and Fig. S5A-D). Under these conditions, cAMP levels were significantly elevated upon the isoproterenol stimulation compared to the basal conditions (Fig. 4C). As *Zip13*-KO mature adipocytes have increased Fe^{2+} in the cytosol, we investigated whether oxidative stress affects PDE activity, which turns out that PDE activity was decreased by H_2O_2 treatment (Fig. 4F). The redox sensitivity of PDE enzymes, including the effect of ROS, has been previously reported (33). PDEs contain multiple cysteine residues that are susceptible to oxidation, which can lead to conformational changes and reduced catalytic activity. Thus, it is reasonable to conclude that ROS-induced cysteine oxidation underlies the suppression of PDE3 activity observed in our study. These results suggest that *Zip13*-KO mature adipocytes have increased Fe^{2+} and increased pro-oxidants in the cytosol, leading to

increased cAMP/PKA activity, which results in the enhancement of NEFA release.

Considering the modest but significant increase in the thermogenic response in Adipo-*Zip13*KO mice (Fig. 2E), we next investigated whether iron distribution and cAMP/PKA signaling pathway activity are altered in mature adipocytes derived from the BAT of these mice. Uncoupling protein 1 (UCP1) protein levels were increased in the BAT of Adipo-*Zip13*KO mice and iron distribution was altered, similar to what was observed in the WAT of these mice (Fig. S6A–C). Consistently, activation of the cAMP/PKA signaling pathway was observed in the BAT of Adipo-*Zip13*KO mice (Fig. S6), supporting enhanced thermogenic activity (Fig. 2E). In parallel, fasting plasma NEFA levels were increased in these mice (Fig. 1D), suggesting elevated lipid mobilization that may contribute to changes in RER and thermogenesis (Fig. 1C and 2E). Enhanced NEFA uptake and oxidation in BAT may facilitate the rapid clearance of circulating NEFAs following β-adrenergic receptor agonist-induced stimulation (Fig. 1D), thereby contributing to increased energy expenditure. Collectively, these results suggest that enhanced BAT thermogenesis contributes to resistance to HFD-induced obesity and improved insulin sensitivity in Adipo-*Zip13*KO mice, further establishing ZIP13 as a regulator of lipid homeostasis and thermogenic responses.

ZIP13 transports both Fe^{2+} and Zn^{2+}

To directly assess ZIP13 transport activity under controlled and quantifiable conditions, we employed the *Xenopus laevis* oocyte assay, in which ZIP13 was ectopically expressed on the plasma

membrane. This system allowed us to investigate the transport activity of Zn^{2+} and Fe^{2+} under defined conditions. Upon injection of complementary RNA (cRNA) of the full-length form of mouse ZIP13 (mZIP13), its protein was mainly expressed in intracellular spaces but not on the cell surface of oocytes (Fig. 5A, upper left). To force the ZIP13 protein to be localized on the plasma membrane, we fused mZIP13 with human SLC3A24/4F2 cell-surface antigen heavy chain (4F2hc), which is a subunit of this large neutral amino acid transporters such as L-type amino acid transporter 1(LAT1) (34) (Fig. 5B). This fusion protein, named 4F2hc-mZIP13-HA (4F2hc-m13), was localized to the plasma membrane of oocytes (Fig. 5A, lower left). Its topology matched that of native ZIP13 (Fig. S7). Similarly, fusion protein 4F2hc-mZIP14-HA (4F2hc-m14), used as a positive control, was also correctly expressed and is known to transport both Zn^{2+} and Fe^{2+} (Fig. 5A, lower right) (16, 17). Three-dimensional structure simulation using Alphafold2 suggested that the structure of the metal transporting regions of 4F2hc-m13 protein was unaffected (Fig. 5C), and both 4F2hc-m13 and 4F2hc-m14 proteins induced the expression of metallothionein 1 gene (*MT1*), an indicator of intracellular zinc level (23, 24, 25) in HEK293 cells (Fig. 5D). These results indicated that both fusion transporters could transport Zn^{2+} into cells. We further assessed these fusion transporters by using *X. laevis* oocytes system, demonstrating that the 4F2hc-m13 protein transports Zn^{2+} and Fe^{2+} (Fig. 5E and F), and that the Km values of Zn^{2+} and Fe^{2+} for the 4F2hc-m13 protein appeared to be almost the same (Fig. S8), clearly showing that ZIP13 can transport both Zn^{2+} and Fe^{2+}.

268 ***In silico* structural dynamics simulations of ZIP13-meditaed metal transport**

269 To investigate the ion-biding properties of ZIP13, we performed molecular dynamics (MD)
270 simulation (Fig. 6A). The ion (Zn^{2+} or Fe^{2+}) was docked to the binuclear metal (M1-M2) binding site
271 of the wild-type form of mouse ZIP13 (ZIP13-WT) predicted by ZincBind web server. To evaluate
272 the ion mobility, the ion at M1 was not restrained during minimization or the production phase of the
273 MD simulations, allowing ions and all atoms of residue to move freely. The ion-binding stability of
274 Zn^{2+} and Fe^{2+} was evaluated using 0.5-μs MD simulations with three independent replicates for each
275 system.

276 This ion-binding analysis shows that both Zn^{2+} and Fe^{2+} at the M2 site could stably bind to
277 ZIP13-WT/Zn^{2+} and ZIP13-WT/Fe^{2+} throughout the MD trajectories in all systems (Fig. 6B and C).
278 The Zn^{2+} and Fe^{2+} show strong binding to N222, D225, N226, and E255 of the ZIP13 protein (Fig.
279 6C) in all modes, similar to what was previously reported in the model of ZIP8 (35). For both Zn^{2+}
280 and Fe^{2+}, the ion at M1 seems to move from M1 (original binding site) site to M1' (outward) site in
281 the early phase of MD simulation. Specifically, in ZIP13-WT/Zn^{2+}, the ion at the M1 site stably bound
282 until 0.17 μs, whereas the ion at the M1 site of the ZIP13-WT/Fe^{2+} system rapidly moved out at about
283 0.05 μs in all replications (Fig. 6B), indicating that ZIP13 retains Zn^{2+} at M1 site longer than Fe^{2+},
284 suggesting a lower energy barrier for Fe^{2} ejection from the ion-binding site. Among the amino acid
285 residues in the M1 and M2 sites, E255 and E259 showed a strong binding interaction with both ions
286 according to the occupancy of the ion at each residue (Fig. 6C). When the ion is released from the

M1 site to M1' site, conformational changes in the side chain of H254 facilitate ion ejection, supporting a critical role for H254 in facilitating ion ejection during ZIP13-mediated transport. In this process, H254 binds Zn^{2+} for slightly longer than Fe^{2+}, which is probably the reason why Fe^{2+} is ejected faster from the ion-binding sites. Consistent with this interpretation, previous studies, including our own, have demonstrated that H254 is a critical residue for regulating zinc dynamics (23, 36).

Together, these simulation data suggest that mammalian ZIP13 is capable of transporting both Zn^{2+} and Fe^{2+}, with preferential retention of Zn^{2+} but faster release of Fe^{2}, whereas functional transport in cells appears to be governed by cellular context, including metal availability and subcellular localization.

ZIP13 harboring loss-of-function mutations affect Zn^{2+} and Fe^{2+} homeostasis

To assess the relevance of the simulation results in a cellular context, we investigated whether the ectopic expression of ZIP13 and its mutant form alters subcellular metal distribution within intracellular organelles in *Zip13*-KO preadipocytes, which were subsequently differentiated into mature adipocytes (23, 36) (Fig. 7A and Fig. S9A). In the preadipocytes, we observed that the expression of ZIP13-WT induced an increase in organelle-associated Zn^{2+} levels, but not Fe^{2+} levels, and this change was reduced by the expression of ZIP13-H254A compared with that of ZIP13-WT (Fig. 7B), suggesting that ZIP13 primary regulates Zn^{2+} in this context.

306 In contrast, in mature adipocytes, ZIP13-WT increased both Zn^{2+} but also Fe^{2+} levels in
307 organelles, whereas the ZIP13-H254A selectively reduced Fe^{2+} levels (Fig. 7C), indicating that ZIP13
308 predominantly mobilized Fe^{2+} in mature adipocytes. These results support a context-dependent shift
309 in substrate utilization of ZIP13 from Zn^{2+} to Fe^{2+} during adipocyte differentiation. We next examined
310 whether ZIP13-mediated metal transport contributes to lipolysis of mature adipocytes, using the
311 mutant ZIP13-H254A, which impaired Fe^{2+} transporting ability in mature adipocytes (Fig. 7C, and
312 S9A). Notably, the ZIP13-H254A mutant failed to suppress NEFA release, unlike ZIP13-WT (Fig.
313 S9B), although adipocyte differentiation efficiency was low in cells expressing ZIP13-WT compared
314 with those expressing ZIP13-H254A (Fig. S9A, and S9C). Given the phenotype of *Zip13* deficient
315 adipocytes, these results suggest that the Fe^{2+} transport ability of ZIP13 might be required for the
316 inhibition of lipolysis in the mature adipocyte.

317 Finally, we investigated the basis for the context-dependent shift in substrate preference of
318 ZIP13 from Zn^{2+} to Fe^{2+} during adipocyte differentiation. Notably, intracellular iron levels are known
319 to be increased during adipocyte differentiation (37, 38). We therefore quantified total zinc and iron
320 levels in both preadipocytes and mature adipocytes. ICP-MS analysis indicated that total iron levels
321 were significantly increased in mature adipocytes, whereas zinc levels were comparable to those in
322 preadipocytes. These differences were not affected by the loss of ZIP13 (Fig. 7D, E and F), indicating
323 that the changes in total metal abundance during adipocyte differentiation occur independently of
324 ZIP13. Collectively, these findings support a model in which ZIP13 functions as a context-dependent

metal transporter, with substrate utilization shifting from Zn^{2+} to Fe^{2+} in response to changes in intracellular metal availability during adipocyte differentiation.

Discussion

Patients with Ehlers-Danlos syndrome spondylodysplastic type 3 (EDSSPD3), caused by loss of ZIP13 function, exhibit lipoatrophy and reduced adipose tissue mass, phenotypes that closely resemble those observed in Adipo-*Zip13*KO mice (22). Previously, we demonstrated that ZIP13-mediated Zn^{2+} transport is essential for inhibiting beige adipocyte differentiation (23). In the present study, we further show that ZIP13 regulates intracellular Fe^{2+} distribution in mature adipocytes, thereby restraining excessive lipolysis and thermogenic (Fig. 8, left). Consistent with this, loss of ZIP13 increases intracellular Fe^{2+} levels and reactive oxygen species (ROS) production, leading to enhanced lipolysis and thermogenesis (Fig. 8, right). Collectively, these findings explain the adipose phenotypes associated with ZIP13 deficiency and establish intracellular metal distribution as a fundamental and previously underappreciated regulatory layer of adipocyte metabolism.

Although ZIP13 has primarily been studied as a zinc transporter, the phenotypes observed in *Zip13*-KO mice and EDSSPD3 patients cannot be fully explained by zinc dysregulation alone. Here, we provide evidence that altered intracellular Fe^{2+} distribution contributes to these phenotypes, indicating that ZIP13 functions beyond zinc metabolism. Notably, impaired collagen hydroxylation previously reported in *Zip13*-deficient models may reflect defective Fe^{2+} transport within the ER/Golgi compartments (26, 39), suggesting that intracellular iron distribution is broadly linked to tissue function.

Mechanistically, we found that disruption of ZIP13-mediated Fe^{2+} distribution leads to increased cytosolic Fe^{2+} and oxidative stress, which enhances β-adrenergic signaling and amplifies lipolysis and thermogenesis in mature adipocytes. Together with the rescue of lipolysis by antioxidant treatment, these findings support a causal link between intracellular iron redistribution and metabolic signaling. The effect was more pronounced in subcutaneous adipose tissue, where the Fe/Zn ratio is higher than in visceral fat (Fig. S10), suggesting that tissue-specific metal availability influences ZIP13 function and downstream metabolic signaling. In addition, ZIP13 deficiency altered mitochondrial Fe^{2+} levels (Fig. S11), further supporting a role for ZIP13 in maintaining intracellular iron homeostasis. These findings collectively indicate that the spatial distribution of iron, rather than its total abundance, is a key determinant of adipocyte metabolic function. Our findings further suggest that subcellular metal distribution represents a general regulatory mechanism linking metal homeostasis to diverse cellular signaling pathways beyond adipocytes.

Our results further reveal that ZIP13 exhibits a context-dependent substrate switch from Zn^{2+} to Fe^{2+} during adipocyte differentiation, reflecting changes in intracellular metal availability. Although ZIP13 has been characterized as a Zn^{2+} transporter, our findings suggest that substrate utilization *in vivo* is not solely determined by intrinsic binding affinity, but is strongly influenced by intracellular metal availability. Zn^{2+} may play a dominant role in early differentiation stages, whereas Fe^{2+} becomes functionally dominant in mature adipocytes. Notably, the concentration of labile Fe^{2+} in the cytosol is estimated to be in the micromolar range, whereas free Zn^{2+} is maintained at much

lower levels (pM-nM) (40, 41). This substantial difference in intracellular availability favors Fe^{2+} transport by ZIP13 under physiological conditions, despite its intrinsic affinity for Zn^{2+}. Consistently, ZIP13 appears to favor Zn^{2+} transport in simplified systems such as oocyte assays and MD simulations. In contrast, it functionally shifts toward Fe^{2+} transport in mature adipocytes, driven by the cellular Fe^{2+}/Zn^{2+} balance.

In addition, we developed a functional assay system using *Xenopus* oocytes in which fusion proteins with plasma membrane–localized proteins are employed, enabling direct evaluation of intracellular transporter activity–particularly for those localized to organelle membranes–which is often difficult to assess in mammalian systems. This platform may facilitate future studies aimed at dissecting the transport mechanisms and substrate specificity of ZIP family members.

In summary, we demonstrate that ZIP13 coordinates intracellular metal distribution to regulate adipocyte metabolism (Fig. 8). More broadly, our findings establish intracellular metal distribution—rather than total metal levels—as a previously unrecognized and fundamental regulatory principle in metabolic control. This conceptual advance redefines the role of metal ions in cellular physiology and establishes intracellular metal distribution as a fundamental determinant of metabolic regulation.

Methods

Animal studies

We used both male and female mice *in vitro* study, and examined male mice *in vivo* study. All mice were housed in specific pathogen-free barrier facilities, maintained under a 12-h light/dark cycle, given water *ad libitum*, and fed standard rodent food (Oriental Yeast, Tokyo, Japan) or rodent food containing 60% fat (Research Diet, New Brunswick, NJ, USA) from 6 to 18 weeks of age (42). 60% HFD is widely used to robustly induce obesity and metabolic stress in mice. *Zip13*^{flox} mice (accession no. CDB1360K: https://large.riken.jp/distribution/mutant-list.html) were generated by using TT2 embryonic stem (ES) cells derived from a hybrid strain between C57BL/6 and CBA (42). To construct a targeting vector, genomic fragments of the *Zip13* locus were obtained from a C57BL/6 BAC clone (BACPAC Resources). A 3.8-kbp region containing from exon 5 to 10 of the *Zip13* gene was flanked by loxP sites (Fig. S12). The targeted ES clones were microinjected into 8-cell stage ICR embryos, and the injected embryos were transferred into pseudopregnant ICR females. The resulting chimeras were crossed with B6;SJL-Tg(ACTFLPe)9205Dym/J mice to remove the drug-resistant Neo and Puro cassettes, and heterozygous offspring were identified by polymerase chain reaction (PCR) using the following primers: P1 (5'-CCA GCC AGGT GAG CCC CAA G-3') and P2 (5'-TTC CGG GCA GAG GGC ACA GT-3') (WT: 1,449 bp; Flox: 1,730 bp), and P3 (5'-ACCGGCTGCCTCTTCCACAT-3') and P4 (5'-GTG CCC CCT GCT GTG TGA GG-3') (WT: 513 bp; Flox: 689 bp). Adiponectin-Cre mice were obtained from Jackson Laboratories (strain no.

010803), and all mice were backcrossed onto C57BL/6J mice for more than seven generations. Adipocyte-specific *Zip13*-KO mice were generated by crossing *Zip13*-flox mice with adiponectin-Cre mice. *Zip13*$^{flox/flox}$*; Adiponectin*-Cre mice were initially used as adipocyte-specific *Zip13*-KO mice. However, as these mice showed no obvious phenotypes associated with mature adipocytes, such as a decrease RER and increase in VO_2, as observed in systemic *Zip13*-KO mice (Fig. S13), *Zip13*$^{flox/-}$*; Adiponectin*-Cre mice were generated and used because of their higher efficiency of ZIP13 deletion than *Zip13*$^{flox/flox}$*; Adiponectin*-Cre mice. In this study, *Zip13*$^{flox/-}$*; Adiponectin*-Cre mice were defined as Adipo-*Zip13*KO mice. Both the phenotypes of *Zip13*-KO mice and the clinical symptoms observed in patients with EDSSPD3 are inherited in an autosomal recessive manner. Because *Zip13* expression in mature adipocytes of *Zip13*$^{flox/+}$*; Adiponectin*-Cre mice is comparable to that in heterozygous (+/–) carriers, which do not display the abnormalities seen in homozygous (–/–) mice, *Zip13*$^{flox/+}$*; Adiponectin*-Cre mice were used as controls.

Metabolic studies

Indirect calorimetry

VO_2 and VCO_2 were measured in individual mice at the indicated ages using an Oxymax apparatus (Columbus Instruments, Columbus, OH, USA). O_2 and CO_2 measurements were performed every 18 min over a 3-day period, during both the light and dark phases, and the data from the final day were analyzed. Locomotor activity was measured in a metabolic chamber using an infrared light beam

detection system (ACTIMO-100; Shinfactory, Fukuoka, Japan). Total locomotor activity during a 12-h period was measured.

Cell immortalization and culture

White preadipocytes were isolated from the subcutaneous fat tissue of Ctrl and Adipo-*Zip13*KO mice (6-8-weeks olds) by collagenase digestion, and then immortalized, as described previously (23). Briefly, preadipocytes were immortalized by retroviral transduction with the SV40 largeT antigen, and selection with puromycin (2 mg/mL). Immortalized preadipocytes were a mixed population, and two cell lines were analyzed. Preadipocytes were seeded onto collagen-coated dishes (Corning, Kennebunk, ME, USA) in Dulbecco's Modified Eagle Medium (DMEM)/F12 (Gibco, Carlsbad, CA, USA) with 10% fetal bovine serum (FBS). For white adipocyte differentiation, cells were induced with induction medium containing 10% FBS, 5 μg/mL insulin (Humalin R, Eli Lilly), 250 μM isobutylmethylxanthine (Sigma-Aldrich, St. Louis, MO, USA), 125 μM indomethacin (Sigma), and 2 μg/mL dexamethasone (Sigma) in DMEM/F12 according to the manufacturer's protocol (43). Two days after induction, the culture medium was changed to a maintenance medium containing 10% FBS and 5 μg/mL insulin. For isoproterenol treatment, cells were incubated with 10 μM isoproterenol for 2 h.

Immunoblotting

Immunoblotting was performed as described previously (23, 44, 45, 46). The following antibodies were used for immunoblotting: anti-Fth1 (1:1,000; Abcam, St. Charles, MO, #EPR3004Y), anti-FTL (1:1,000; Abcam, #ab69090), anti-IRP2 (1:1,000; Millipore, Bedford, MA, USA, #MABS2030), anti-TfR (1:1,000; Invitrogen, Carlsbad, CA, USA, #136890), anti-adipocyte Protein 2 (aP2) (1:1,000; Cell Signaling, Danvers, MA, #2120), anti-actin (1:5,000; Sigma, #A2228), anti-pPKA (1:1,000; Cell Signaling, #5661), anti-PKA (1:1,000; Cell Signaling, #5842), anti-pHSL(Ser563) (1:1,000; Invitrogen, #PA5-17488), anti-pHSL(Ser565) (1:1,000; Cell Signaling, #4137), anti-pHSL(Ser660) (1:1,000; Cell Signaling, #45804), anti-HSL (1:1000; Cell Signaling, #4107), anti-pCREB (1:1,000; Cell Signaling, #9198), anti-CREB (1:1,000; Cell Signaling, #9197), and anti-GAPDH (1:3,000; Cell Signaling, #2118).

Immunofluorescence experiments

X. laevis oocytes injected with cRNAs were fixed with paraformaldehyde and embedded in paraffin. The sliced sections were incubated with an anti-HA monoclonal antibody (1:1000; BioLegend, San Diego, CA, USA, #901514), followed by anti-mouse Alex Fluor 488-conjugated immunoglobulin (1:100; Thermo Fisher Scientific). The sections were mounted in fluorescence mounting medium (Nacalai Tesque, Kyoto, Japan). Fluorescence was visualized using an Olympus Fluoview FV1000 laser confocal microscope. Images are the product of 3-fold line averaging. Immunofluorescence experiments using preadipocytes were as described previously (23, 44, 47). The following antibodies

were used: anti-GM130 (1:250; Transduction Laboratories, Lexington, KY, USA, #610823), anti-calreticulin (1:250; Thermo Fisher Scientific, #PA3-900), and anti-HA (1:250; BioLegend, San Diego, CA, USA, #901513) or anti-HA (1:100; MBL, #561).

Gene expression analysis

Total RNA was isolated from tissues using QIAzol (Qiagen, Valencia, CA, USA) following the manufacturer's protocol. Reverse transcription reactions were performed using High Capacity cDNA Synthesis Kit (Applied Biosystems, Foster, CA, USA). The sequences of the primers used in this study are shown in Table S1. Quantitative reverse transcriptase polymerase chain reaction (qRT-PCR) was performed with SYBR green-fluorescent dye using an ABI 7500 Fast Real-Time PCR System. Relative mRNA expression was determined by relative standard curve methods using *18S* (for mouse), or *Gapdh* (for human) as an internal control to normalize samples.

Plasmid construction and virus production

C-terminally HA-tagged plasmids expressing mouse ZIP13 (mZIP13-HA) were as described previously (23). PLAT-E packaging cells were transfected using retroviral vectors by lipofection. After 48 h, the viral supernatant was collected and filtered. Preadipocytes were incubated for 6 h with viral supernatant supplemented with 10 μg/mL polybrene. For the construction of 4F2hc-m13 and 4F2hc-m14, 4F2hc and mZIP13 or mZIP14 were fused by PCR and In-Fusion® HD Cloning Kit

(Takara Bio, Shiga, Japan), according to the manufacturer's instructions. In-Fusion PCR primers were designed to share 15 bases of homology with the PCR fragments and vector ends. 4F2hc, ZIP13 and ZIP14 plasmids, which had already been constructed previously (23, 34, 48), were used for the PCR templates. The PCR fragments were subcloned into the mammalian expression vector pcDNA 3.1(-) at an EcoRV site.

In vivo and *ex vivo* lipolysis assay

To determine *in vivo* lipolysis, circulating plasma NEFA levels were measured after overnight fasting (12 h). Mice were then given an intraperitoneal (i.p.) injection of 1mg/kg CL316,243 (Sigama). Plasma NEFAs were measured 30 min after the injection. CL316,243 was chosen due to its high β3-adorenoceptor selectivity in mouse adipose tissue, allowing specific assessment of adipose-derived lipolysis. To determine *ex vivo* lipolysis, the release of NEFA from adipose tissues was measured, as previously described (47). Briefly, mice were sacrificed, and each type of adipose tissue was excised. The fat pads were washed in prewarmed 2% bovine serum albumin (BSA, free fatty acid free)-DMEM/F12 medium. Adipose tissue pieces (20 mg) were incubated in 200 μL 2% BSA-DMEM/F12 medium with 5μM triacsin C (Sigma) in the presence or absence of 10 μM isoproterenol. The medium was removed and used to measure NEFA release using a NEFA kit (WAKO, Tokyo, Japan). For protein quantification, fat explants were first incubated in 1 mL extraction solution (chloroform: methanol, 2:1) and incubated for 60 min at 37 °C under vigorous shaking. Then, the tissue pieces

were transferred to 500 µL lysis solution (0.3 N NaOH/0.1% sodium dodecyl sulfate (SDS)) and incubated overnight at 55 °C under vigorous shaking. Protein content was determined using Pierce 660 nm protein assay reagent (Thermo Fisher Scientific), and BSA as the standard.

For the lipolysis assay using mature adipocytes, subcutaneous and visceral adipose tissues were harvested from mice and minced, followed by collagenase digestion for 45 min using type I collagenase (1 mg/mL; Worthington Biochemical Corporation, Lakewood, NJ, USA) in Krebs-Ringer bicarbonate (KRB) buffer supplemented with 2% BSA, as described previously. Mature adipocytes were then collected and washed four times with KRB buffer containing 2% BSA to remove residual collagenase. The cells were resuspended in an appropriate volume of KRB buffer containing 2% BSA, and after centrifugation, the cytocrit was measured using hematocrit capillary tubes. Lipolysis assays were performed as previously described. Briefly, adipocytes were incubated for 20 min at 37 °C, after which the reaction was stopped to obtain the baseline value (pretreatment value). The cells were then further incubated for 60 min in the presence or absence of isoproterenol, and the reaction was terminated to obtain the end value. Lipolysis during the 60-min incubation period was calculated as the difference between the end value and the pretreatment value. The levels of NEFAs released into the incubation medium were measured using the commercial kit described above, according to the manufacturer's instructions.

Cellular lipolysis assay

Preadipocytes were incubated with a differentiation induction cocktail, and differentiated for 8 days. Lipolysis was assessed by measuring NEFA release in the culture medium. The NEFA assay was performed according to the manufacturer's instructions (49). Briefly, aliquots of cell culture medium (4μL) were added to 80 μL reagent A, and incubated at 37 °C for 10 min. This was followed by the addition of 160 μL reagent B, and incubation for another 37 °C for 10 min, and then absorbance was measured at 550 nm. NEFA release was normalized to total protein content using Pierce 660 nm Protein Assay Reagent.

cAMP analysis

The cAMP enzyme immunoassay (Cayman) was performed according to the manufacture's protocol. Briefly, preadipocytes were differentiated into mature adipocytes, and treated with 10 μM isoproterenol, and then cells were washed twice with ice-cold phosphate-buffer saline (PBS), lysed by the addition of 1 mL 0.1 M HCl, and centrifuged at 1,000 *g* for 10 min. The supernatant was diluted in enzyme-linked immunosorbent assay (ELISA) buffer (sample dilution: x3) and cAMP levels were measured by enzyme immunoassay according to the manufacturer's protocol. cAMP levels were normalized to protein content, which was determined by assaying the supernatant using the pierce 660 nm protein assay reagent.

PDE activity assay

PDE activity was measured using the PDE activity assay kit according to the manufacturer's protocol (Abcam). PDE activity was normalized to protein content, by assaying the cell lysates using Pierce 660 nm Protein Assay Reagent.

Zn^{2+} and Fe^{2+} measurements

Zn^{2+} levels were measured using FluoZin-3 (Invitrogen, #F24194) as described previously (24). Cells were plated onto 24-well plates, and washed with Hanks' Balanced Salt Solution (HBSS) buffer (Sigma-Aldrich) 3 times. The cells were then incubated with 3 μM FluoZin-3 for 1 h, and washed with HBSS buffer 3 times. Fluorescence was recorded at 495 nm excitation and 517 nm emission using EnSpire multimode plate reader (Perkin Elmer). Fe^{2+} levels were measured using FerroOrange (DOJINDO, Kumamoto, Japan, #F374) as described previously (50). Briefly, the cells were incubated with 2 μM FerroOrange for 1 h. Fluorescence was recorded at 543 nm excitation and 580 nm emission. For protein determination, cells were lysed with 250 μL lysis solution (0.3N NaOH/0.1% SDS), and incubated at room temperature under vigorous shaking. Then, protein content was determined using Pierce 660 nm Protein Assay Reagent and BSA as a standard.

cRNA preparation

Oocyte expression vectors were linearized with Hind III and *in-vitro* transcribed to cRNA using the mMESSAGE mMACHINE T7 Transcription Kit (Thermo Fisher Scientific). Synthesized cRNAs

were then polyadenylated with the Poly(A) Tailing Kit (Thermo Fisher Scientific) and purified with the MEGAclear Transcription Clean-Up Kit (Thermo Fisher Scientific), according to the manufacturer's protocols.

Oocyte preparation and transporter expression

The oocyte transport assay was performed as previously reported (51). This system allows precise control of subcellular localization and has been used in many studies characterizing intracellular transporters (52, 53). Briefly, adult female *X. laevis* (Watanabe Zoshoku, Japan) were anesthetized with 1.0 to 1.5 mg/mL tricaine (Tokyo Chemical Industry, Japan) and pieces of the ovary were surgically removed. Oocytes were isolated from the ovary and defolliculated with 1.0 to 1.5 mg/mL collagenase A (Roche, Basel, Switzerland) in OR2 buffer (82 mM NaCl, 2.5 mM KCl, 1 mM $MgCl_2$, 5 mM HEPES; pH 7.6) at room temperature for 1.5 to 2 h. Defolliculated oocytes were washed more than 5 times with OR2 buffer, and then transferred to ND96 buffer (96 mM NaCl, 2 mM KCl, 1.8 mM $CaCl_2$, 1 mM $MgCl_2$, 5 mM HEPES; pH 7.5). Stage IV to VI oocytes were selected and injected with 18.4 nL (18.4 ng) of purified cRNAs, or equal volumes of RNA-free water using Nanoject II microinjector (Drummond Scientific, PA, USA), and incubated for 2 days at 18 °C in ND96 buffer before their use in the uptake assay.

Metal uptake assay

Six to eight cRNA-injected oocytes were placed in a 96-well plate, and washed twice with ND96 buffer. The iron uptake assay was started by replacing the buffer with 120 μL of ND96 buffer containing 100 μM $FeCl_2$, 1 to 5 μCi/mL $^{55}FeCl_3$ (Perkin Elmer), and 1 mM ascorbic acid and incubated at 22 °C for 240 min. The uptake was stopped by replacing the uptake solution with ice-cold ND96 supplemented with 1 mM ascorbic acid. The oocytes were then transferred to a 24-well plate and washed 5 times with the same buffer, solubilized with 0.0625 N NaOH, and radioactivity was measured by liquid scintillation counting. The zinc uptake assay was started by replacing the buffer with 120 μL of ND96 containing 100 μM $ZnSO_4$ and 1 to 2 μCi/mL $^{65}ZnCl_2$ (RIKEN, Japan). The uptake was stopped by replacing the uptake solution with ice-cold ND96 buffer supplemented with 5 mM EDTA. Oocytes were transferred to a 24-well plate and washed 5 times with the same buffer. The amount of zinc in the oocytes was visualized by a Phosphor Imager (Typhoon FLA 9500; GE Healthcare, IL, USA), and quantified by ImageJ software. Each experiment was performed twice on different days.

Structure prediction

Protein structure prediction of 4F2hc-m13 was performed using a locally installed version of ColabFold v1.3.0 (54), which is the optimized implementation version of the AlphaFold2. Five models of 4F2hc-m13 were generated with 3 recycles, and refined with AMBER force field. The models were visualized and superimposed with the model of mouse ZIP13 (PDB ID: Q8BZH0)

deposited in AlphaFold DB using Mol* Viewer (Fig. S13) (55). The predicted models were ranked by their predicted local distance difference test value (a per-residue confidence score), and the m13 domain of the top-scored model (rank 1) was superimposed with the m13 domains of the other models (Fig. S14).

ICP-MS

Preadipocyte and mature adipocytes were harvested with methanol, and then the methanol was evaporated by centrifugal concentration (56). Samples were digested with 0.5 mL of HNO_3 (Tamapure-AA-100, Tama Chemical Co. Ltd., Kanagawa, Japan) at 180 °C for 20 min in an ETHOS 1 microwave oven (Milestone, Srl, Sorisole, Italy) and then diluted with ultra-pure water (manufactured by PURELAB Option-R 7 and PURELAB flex UV, Veolia Water Solution and Technologies, Paris, France) to a final volume of 5mL. Concentrations of Fe and Zn were determined using inductively coupled plasma-sector field mass spectrometry ICP-SFMS (ELEMENT XR, Thermo Fisher Scientific Inc., Bremen, Germany). ^{56}Fe and ^{66}Zn were measured using medium resolution mode (R = 4,000). The methanol blank samples were prepared without cells and analyzed in the same manner. The amounts of Fe and Zn were corrected by subtracting the mean amounts of the blank samples.

Ion binding site prediction and analysis

608 The 3D structure of mouse ZIP13 (ZIP13-WT), obtained from the AlphaFold2 database (UniProt ID:
609 Q8BZH0) (57), was used as the structure for ion-binding prediction. Structural pairwise alignment
610 between ZIP8, sourced from a previous study (35) and ZIP13, together with the ZincBind web server
611 (58), facilitated the prediction and confirmation of the two ion coordination sites denoted as M1 and
612 M2. Subsequently, homo Zn^{2+} ions were positioned within M1 and M2 in ZIP13-WT. This
613 methodology was also used for homo Fe^{2+} system preparation. The parameters of the modified 12-6-
614 4 Lennard-Jones (m-12-6-4-LJ) non-bonded model for Zn^{2+} and Fe^{2+} were adopted based on previous
615 recommendations (35). The previous m-12-6-4-LJ model was developed to incorporate the
616 polarizabilities of the coordinating atoms, which is crucial for accurately capturing the induced dipole
617 effect in MD simulations of ion transport involving metal ions and coordinating atoms (59, 60, 61).
618 This model was also validated for its effectiveness in simulating metal binding at the selectivity filter,
619 highlighting its sensitivity to the polarizability of coordinating atoms. Both ZIP13-WT complexes
620 with Zn^{2+} and Fe^{2+} were simulated for 0.5-μs MD trajectories with 3 independent replications, each
621 starting with different velocities, to observe ion binding stability using AMBER20 package software
622 (62), as a standard protocol (63, 64). These systems were prepared for 0.5-μs MD simulations via
623 CHARMM-GUI (65), featuring box dimensions of $99 \times 99 \times 123$ Å, with 131 1,2-dilauroyl-sn-
624 glycero-3-phosphocholine (DLPC) molecules per leaflet, and 27,442 TIP3P water molecules. System
625 neutralization was achieved using a 0.15 M KCl concentration, with an additional 0.05 M ZnCl and
626 0.05 M FeCl added to the system with ZIP13/Zn^{2+} and ZIP13/Fe^{2+}, respectively. Protein and ions

were treated by ff19SB Amber forcefield (66) and 12-6-4 Lennard-Jones model, respectively. Five-step minimization, utilizing steepest descent and conjugate gradient methods with restriction from the protein backbone to the side chain, was conducted for 10,000 steps at each stage. Subsequently, a 36- ns NVT heating phase gradually increased the temperature from 0 to 300 K. Production involved 0.5- μs MD simulations. These MD trajectories were analyzed to assess ion-binding stability by the "hbond" action command implemented in the CPPTRAJ (67) module within the AmberTools 21 package program (68). This technique resembles traditional hydrogen bond interaction analysis but with the angle cutoff disabled and the distance cutoff set at 3.0 Å. The evaluation of ion-binding stability was based on the total number of ion-binding contacts throughout the simulation and the average number of amino acids in contact with the ions.

AI use

ChatGPT (Open AI, San Francisco, CA, USA) was used to assist in improving the readability of the manuscript and to refine R code. The authors take full responsibility for the content of the manuscript, including all parts written with assistance of the AI tool.

Statistical analysis

All quantitative data were reported as the mean ± standard error of the mean (SEM). Statistical differences between the two groups were analyzed by the two-tailed unpaired Student *t*-test. The

multiple comparisons were performed by one-way ANOVA with the post-hoc Tukey-Kramer test for comparisons among groups, or the post-hoc Dunnett test for the comparison of groups with a specific control, or two-way ANOVA with the Bonferroni's multiple comparison test. A *p*-value of less than 0.05 was considered to indicate a statistically significant difference between groups.

Ethics approval

All animal experiments were performed in accordance with the institutional and national guidelines and regulations, and RIKEN Regulations for the Animal Experiments. The study protocol was approved by the Institutional Animal Care and Use Committee of Gunma University (study approval no.: #19-025), and of RIKEN Kobe Branch (study approval no: A2001-03). This study was reported in accordance with ARRIVE guidelines.

Acknowledgments

We thank Prof. T. Nishimura, for fruitful discussions and critical comments on the manuscript, Dr. H. A. Popiel, Dr. A. Iizuka, Dr. I. Yanatori, Dr. K. Muranishi, Dr. D. Kato, Professor T. Inagaki, Professor K. Ishimori, Professor Y. Tamura, and Professor S. Nagamori, for their helpful suggestions and discussions, and Ms. Y. Miyazaki, Ms. Y. Tamura, Ms. W. Mizutani, and Ms. A. Suda for their technical assistance. We also appreciate the assistance from the Mouse Facility Core of Gunma University. This work was supported by a Grant-in-Aid for Scientific Research on Innovative Areas "Integrated Bio-metal Science" (MEXT KAKENHI grant no. 22H04801 to A.F.), and grant no. 26H00433, 22K8618, and 19K08971 (to A.F.), 20H03409 (to T.F.) and 25K03059 (to Y.F.) from the Ministry of Education, Culture, Sports, Science, and Technology, Japan; grants from The Koyanagi Foundation, The TANITA Healthy Weight Community Trust, Kanae Foundation for the Promotion of Medical Science, Front Runner of Future Diabetes Research Foundation, the Shiseido Female Researcher Science Grant, The Cell Science Research Foundation, The Ichiro Kanehara Foundation, The Nakatomi Foundation, LOTTE Foundation, The Sugiyama Chemical & Industrial Laboratory, Gunma University for the Promotion of Scientific Research (all to A.F.), and from Takeda Science Foundation (to A.F., T.F. and Y.F.). This work was also supported by a research grant from the Secom Science and Technology Foundation (to Y.F.). This work was carried out by the joint research program of the Institute for Molecular and Cellular Regulation, Gunma University (grant no. 18010 to T.F., grant no. 24016 to G.T.). The *in silico* ion-binding site study was performed with support from MEXT

676 Japan (grant no. 22H04800), JST CREST (grant no. JPMJCR20B3), JSPS Grant-in-Aid for Early-
677 Career Scientists (grant no. 24K20888), and the Cooperative Research Program at CCS, University
678 of Tsukuba, and the Quantum Information LifeScience Project.

679 **Author contributions**

680 A.F. conceived the project, performed the experiments, and analyzed the data. G.T. and T.K.
681 performed the oocyte transport experiments. A.F. and D.S. conducted the metabolic studies. K.H.
682 performed the *in silico* study of ion-binding site evaluation. T.I. performed the ICP-MS analysis. M.
683 Shimura, I.A., T.S., and Y.N. analyzed the data. M. Shigeta, H.K., and T.F. generated the *Zip13*-flox
684 mice. T.H. and I.H. provided Adiponectin-Cre mice. A.F. wrote the original manuscript, and A.F., H.
685 Shibata, K.H., Y.S., H. Sakurai, S.K., H.W., T.F., and Y.F. reviewed the manuscript. T.F. and Y.F.
686 supervised the project.

687

688 **Declaration of conflicts of interest**

689 The authors declare no competing interests in association with this study.

690

691 **References**

692 1 Auger, C. & Kajimura, S. Adipose Tissue Remodeling in Pathophysiology. *Annu Rev*
693 *Pathol* **18**, 71-93 (2023). https://doi.org/10.1146/annurev-pathol-042220-023633
694 2 Angueira, A. R. *et al.* Defining the lineage of thermogenic perivascular adipose tissue.
695 *Nat Metab* **3**, 469-484 (2021). https://doi.org/10.1038/s42255-021-00380-0
696 3 Betz MJ, and Enerback S. Targeting thermogenesis in brown fat and muscle to
697 treat obesity and metabolic disease. *Nat Rev Endocrinol.* 2018;14(2):77-87.
698 4 Tamaki, M. *et al.* The diabetes-susceptible gene SLC30A8/ZnT8 regulates hepatic
699 insulin clearance. *J Clin Invest* **123**, 4513-4524 (2013).
700 https://doi.org/10.1172/JCI68807
701 5 Misu, H. *et al.* Deficiency of the hepatokine selenoprotein P increases responsiveness
702 to exercise in mice through upregulation of reactive oxygen species and AMP-activated
703 protein kinase in muscle. *Nat Med* **23**, 508-516 (2017). https://doi.org/10.1038/nm.4295
704 6 Jiang, J. *et al.* Thermogenic adipocyte-derived zinc promotes sympathetic innervation
705 in male mice. *Nat Metab* **5**, 481-494 (2023). https://doi.org/10.1038/s42255-023-
706 00751-9
707 7 Fukunaka, A. & Fujitani, Y. Role of Zinc Homeostasis in the Pathogenesis of Diabetes
708 and Obesity. *Int J Mol Sci* **19** (2018). https://doi.org/10.3390/ijms1902047699
709 8 Maret, W. Zinc in Pancreatic Islet Biology, Insulin Sensitivity, and Diabetes. *Prev Nutr*
710 *Food Sci* **22**, 1-8 (2017). https://doi.org/10.3746/pnf.2017.22.1.1
711 9 Rouault, T. A. Iron metabolism in the CNS: implications for neurodegenerative diseases.
712 *Nat Rev Neurosci* **14**, 551-564 (2013). https://doi.org/10.1038/nrn3453
713 10 Bogdan, A. R., Miyazawa, M., Hashimoto, K. & Tsuji, Y. Regulators of Iron Homeostasis:
714 New Players in Metabolism, Cell Death, and Disease. *Trends Biochem Sci* **41**, 274-286
715 (2016). https://doi.org/10.1016/j.tibs.2015.11.012
716 11 Simcox, J. A. & McClain, D. A. Iron and diabetes risk. *Cell Metab* **17**, 329-341 (2013).
717 https://doi.org/10.1016/j.cmet.2013.02.007
718 12 Harrison, A. V., Lorenzo, F. R. & McClain, D. A. Iron and the pathophysiology of
719 diabetes. *Annu Rev Physiol* **85**, 339-362 (2023). https://doi.org/10.1146/annurev-
720 physiol-022522-102832
721 13 Krishnamoorthy, L. *et al.* Copper regulates cyclic-AMP-dependent lipolysis. *Nat Chem*
722 *Biol* **12**, 586-592 (2016). https://doi.org/10.1038/nchembio.2098

14 Joffin, N. *et al.* Adipose tissue macrophages exert systemic metabolic control by manipulating local iron concentrations. *Nat Metab* **4**, 1474-1494 (2022). https://doi.org/10.1038/s42255-022-00664-z

15 Jeong, J. & Eide, D. J. The SLC39 family of zinc transporters. *Mol Aspects Med* **34**, 612-619 (2013). https://doi.org/10.1016/j.mam.2012.05.011

16 Jenkitkasemwong, S. *et al.* SLC39A14 is required for the development of hepatocellular iron overload in murine models of hereditary hemochromatosis. *Cell Metab* **22**, 138-150 (2015). https://doi.org/10.1016/j.cmet.2015.05.002

17 Wang, G. *et al.* Metastatic cancers promote cachexia through ZIP14 upregulation in skeletal muscle. *Nat Med* **24**, 770-781 (2018). https://doi.org/10.1038/s41591-018-0054-2

18 Lin, W. *et al.* Hepatic metal ion transporter ZIP8 regulates manganese homeostasis and manganese-dependent enzyme activity. *J Clin Invest* **127**, 2407-2417 (2017). https://doi.org/10.1172/JCI90896

19 Park, J. H. *et al.* SLC39A8 Deficiency: A Disorder of Manganese Transport and Glycosylation. *Am J Hum Genet* **97**, 894-903 (2015). https://doi.org/10.1016/j.ajhg.2015.11.003

20 Scheiber, I. F., Wu, Y., Morgan, S. E. & Zhao, N. The intestinal metal transporter ZIP14 maintains systemic manganese homeostasis. *J Biol Chem* **294**, 9147-9160 (2019). https://doi.org/10.1074/jbc.RA119.008762

21 Jeong, J. *et al.* Promotion of vesicular zinc efflux by ZIP13 and its implications for spondylocheiro dysplastic Ehlers-Danlos syndrome. *Proc Natl Acad Sci USA* **109**, E3530-3538 (2012). https://doi.org/10.1073/pnas.1211775110

22 Fukada, T. *et al.* The zinc transporter SLC39A13/ZIP13 is required for connective tissue development; its involvement in BMP/TGF-β signaling pathways. *PLoS One* **3**, e3642 (2008). https://doi.org/10.1371/journal.pone.0003642

23 Fukunaka, A. *et al.* Zinc transporter ZIP13 suppresses beige adipocyte biogenesis and energy expenditure by regulating C/EBP-β expression. *PLoS Genet* **13**, e1006950 (2017). https://doi.org/10.1371/journal.pgen.1006950

24 Bin, B. H. *et al.* Biochemical characterization of human ZIP13 protein: a homo-dimerized zinc transporter involved in the spondylocheiro dysplastic Ehlers-Danlos syndrome. *J Biol Chem* **286**, 40255-40265 (2011).

https://doi.org/10.1074/jbc.M111.256784

25 Bin, B. H. *et al.* Molecular pathogenesis of spondylocheirodysplastic Ehlers-Danlos syndrome caused by mutant ZIP13 proteins. *EMBO Mol Med* **6**, 1028-1042 (2014). https://doi.org/10.15252/emmm.201303809

26 Giunta, C. *et al.* Spondylocheiro dysplastic form of the Ehlers-Danlos syndrome-an autosomal-recessive entity caused by mutations in the zinc transporter gene SLC39A13. *Am J Hum Genet* **82**, 1290-1305 (2008). https://doi.org/10.1016/j.ajhg.2008.05.001

27 Roebroek AJ, Taylor NA, Louagie E, Pauli I, Smeijers L, Snellinx A, et al. Limited redundancy of the proprotein convertase furin in mouse liver. *J Biol Chem.* 2004;279(51):53442-50.

28 Yousefzadeh MJ, Huerta Guevara AP, Postmus AC, Flores RR, Sano T, Jurdzinski A, et al. Failure to repair endogenous DNA damage in beta-cells causes adult-onset diabetes in mice. *Aging Biol.* 2023;1(1).

29 Xiao, G., Wan, Z., Fan, Q., Tang, X. & Zhou, B. The metal transporter ZIP13 supplies iron into the secretory pathway in *Drosophila melanogaster*. *Elife* **3**, e03191 (2014). https://doi.org/10.7554/eLife.03191

30 Hirayama T, et al. A highly selective turn-on fluorescent probe for iron (II) to visualize labile iron in living cells. *Chemical Science* **3**, (2013). https://doi.org/10.1039/C2SC21649C

31 Rumberger, J. M., Peters, T., Jr., Burrington, C. & Green, A. Transferrin and iron contribute to the lipolytic effect of serum in isolated adipocytes. *Diabetes* **53**, 2535-2541 (2004). https://doi.org/10.2337/diabetes.53.10.2535

32 Grabner, G. F., Xie, H., Schweiger, M. & Zechner, R. Lipolysis: cellular mechanisms for lipid mobilization from fat stores. *Nat Metab* **3**, 1445-1465 (2021).

33 Makino, H., de Buschiazzo, P. M., Pointer, R. H., Jordan, J. E. & Kono, T. Characterization of insulin-sensitive phosphodiesterase in fat cells. I. Effects of salts and oxidation-reduction agents. *J Biol Chem* **255**, 7845-7849 (1980).

34 Kanai, Y. *et al.* Expression cloning and characterization of a transporter for large neutral amino acids activated by the heavy chain of 4F2 antigen (CD98). *J Biol Chem* **273**, 23629-23632 (1998). https://doi.org/10.1074/jbc.273.37.23629

35 Jiang, Y. *et al.* Rational engineering of an elevator-type metal transporter ZIP8 reveals a conditional selectivity filter critically involved in determining substrate specificity. *Commun Biol* **6**, 778 (2023). https://doi.org/10.1038/s42003-023-05146-w

36 Zhang, T. *et al.* Crystal structures of a ZIP zinc transporter reveal a binuclear metal center in the transport pathway. *Sci Adv* **3**, e1700344 (2017). https://doi.org/10.1126/sciadv.1700344

37 Joffin, N. *et al.* Mitochondrial metabolism is a key regulator of the fibro-inflammatory and adipogenic stromal subpopulations in white adipose tissue. *Cell Stem Cell* **28**, 702-717 e708 (2021). https://doi.org/10.1016/j.stem.2021.01.002

38 Moreno-Navarrete, J. M., Ortega, F., Moreno, M., Ricart, W. & Fernandez-Real, J. M. Fine-tuned iron availability is essential to achieve optimal adipocyte differentiation and mitochondrial biogenesis. *Diabetologia* **57**, 1957-1967 (2014). https://doi.org/10.1007/s00125-014-3298-5

39 Li, H. *et al.* Mammalian SLC39A13 promotes ER/Golgi iron transport and iron homeostasis in multiple compartments. *Nat Commun* **15**, 10838 (2024). https://doi.org/10.1038/s41467-024-55149-2

40 Liu R, Kowada T, Du Y, Amagai Y, Matsui T, Inaba K, and Mizukami S. Organelle-Level Labile Zn(2+) Mapping Based on Targetable Fluorescent Sensors. *ACS Sens.* 2022;7(3):748-57.

41 Philpott, C. C., Patel, S. J. & Protchenko, O. Management versus miscues in the cytosolic labile iron pool: The varied functions of iron chaperones. *Biochim Biophys Acta Mol Cell Res* **1867**, 118830 (2020). https://doi.org/10.1016/j.bbamcr.2020.118830

42 Yagi, T. *et al.* A novel ES cell line, TT2, with high germline-differentiating potency. *Anal Biochem* **214**, 70-76 (1993). https://doi.org/10.1006/abio.1993.1458

43 Hausman, D. B., Park, H. J. & Hausman, G. J. Isolation and culture of preadipocytes from rodent white adipose tissue. *Methods Mol Biol* **456**, 201-219 (2008). https://doi.org/10.1007/978-1-59745-245-8_15

44 Shigihara, N. *et al.* Human IAPP-induced pancreatic beta cell toxicity and its regulation by autophagy. *J Clin Invest* **124**, 3634-3644 (2014). https://doi.org/10.1172/JCI69866

45 Fukunaka, A. *et al.* Tissue nonspecific alkaline phosphatase is activated via a two-step mechanism by zinc transport complexes in the early secretory pathway. *J Biol Chem* **286**, 16363-16373 (2011). https://doi.org/10.1074/jbc.M111.227173

46 Fukunaka, A. *et al.* Demonstration and characterization of the heterodimerization of ZnT5 and ZnT6 in the early secretory pathway. *J Biol Chem* **284**, 30798-30806 (2009). https://doi.org/10.1074/jbc.M109.026435

47 Fukunaka, A. *et al.* Zinc and iron dynamics in human islet amyloid polypeptide-induced

diabetes mouse model. *Sci Rep* **13**, 3484 (2023). https://doi.org/10.1038/s41598-023-30498-y

48 Hojyo, S. *et al.* The zinc transporter SLC39A14/ZIP14 controls G-protein coupled receptor-mediated signaling required for systemic growth. *PLoS One* **6**, e18059 (2011). https://doi.org/10.1371/journal.pone.0018059

49 Schweiger, M. *et al.* Measurement of lipolysis. *Methods Enzymol* **538**, 171-193 (2014). https://doi.org/10.1016/B978-0-12-800280-3.00010-4

50 Hirayama, T. Fluorescent probes for the detection of catalytic Fe(II) ion. *Free Radic Biol Med* **133**, 38-45 (2019). https://doi.org/10.1016/j.freeradbiomed.2018.07.004

51 Jutabha, P. *et al.* Human sodium phosphate transporter 4 (hNPT4/SLC17A3) as a common renal secretory pathway for drugs and urate. *J Biol Chem* **285**, 35123-35132 (2010). https://doi.org/10.1074/jbc.M110.121301

52 Uldry M, Ibberson M, Horisberger JD, Chatton JY, Riederer BM, and Thorens B. Identification of a mammalian H(+)-myo-inositol symporter expressed predominantly in the brain. *EMBO J.* 2001;20(16):4467-77.

53 Buracco S, Peracino B, Cinquetti R, Signoretto E, Vollero A, Imperiali F, et al. Dictyostelium Nramp1, which is structurally and functionally similar to mammalian DMT1 transporter, mediates phagosomal iron efflux. *J Cell Sci.*

54 Mirdita, M. *et al.* ColabFold: making protein folding accessible to all. *Nat Methods* **19**, 679-682 (2022). https://doi.org/10.1038/s41592-022-01488-1

55 David Sehnal, et al. Mol* Viewer: modern web app for 3D visualization and analysis of large biomolecular structures. *Nucleic Acids Res* **49**, W431–W437 (2021). https://doi.org/10.1093/nar/gkab314

56 Shimura, M. *et al.* Imaging of intracellular fatty acids by scanning X-ray fluorescence microscopy. *FASEB J* **30**, 4149-4158 (2016). https://doi.org/1o.1096/fj.201600569R

57 Jumper, J. *et al.* Highly accurate protein structure prediction with AlphaFold. *Nature* **596**, 583-589 (2021). https://doi.org/10.1038/s41586-021-03819-2

58 Ireland, S. M. & Martin, A. C. R. ZincBind-the database of zinc binding sites. *Database* (*Oxford*) **2019** (2019). https://doi.org/10.1093/database/baz006

59 Parise, A. & Magistrato, A. Assessing the mechanism of fast-cycling cancer-associated mutations of Rac1 small Rho GTPase. *Protein Sci* **33**, e4939 (2024). https://doi.org/10.1002/pro.4939

60 Puyo-Fourtine, *et al.* Consistent picture of phosphate–divalent cation binding from

models with implicit and explicit electronic polarization. *J Phys Chem B* **126**, 4022-4034 (2022). https://doi.org/10.1021/acs.jpcb.2c01158

61 Mels, O. *et al.* Benchmarking biomolecular force field-based Zn^{2+} for mono- and bimetallic ligand binding sites. *J Comput Chem* **44**, 912-926 (2023). https://doi.org/10.1002/jcc.27052

62 D.A. Case, K. B., I.Y. Ben-Shalom, S.R. Brozell, D.S. Cerutti, T.E. Cheatham, III, V.W.D. Cruzeiro, T.A. Darden, R.E. Duke, G. Giambasu, M.K. Gilson, H. Gohlke, A.W. Goetz, R. Harris, S. Izadi, S.A. Izmailov, K. Kasavajhala, A. Kovalenko, R. Krasny, T. Kurtzman, T.S. Lee, S. LeGrand, P. Li, C. Lin, J. Liu, T. Luchko, R. Luo, V. Man, K.M. Merz, Y. Miao, O. Mikhailovskii, G. Monard, H. Nguyen, A. Onufriev, F.Pan, S. Pantano, R. Qi, D.R. Roe, A. Roitberg, C. Sagui, S. Schott-Verdugo, J. Shen, C.L. Simmerling, N.R.Skrynnikov, J. Smith, J. Swails, R.C. Walker, J. Wang, L. Wilson, R.M. Wolf, X. Wu, Y. Xiong, Y. Xue, D.M. York and P.A. Kollman. *AMBER 2020*. (2020).

63 Hengphasatporn, K. *et al.* Promising SARS-CoV-2 main protease inhibitor ligand-binding modes evaluated using LB-PaCS-MD/FMO. *Scientific Reports* **12**, 17984 (2022). https://doi.org/10.1038/s41598-022-22703-1

64 Hengphasatporn, K. *et al.* Halogenated baicalein as a promising antiviral agent toward SARS-CoV-2 main protease. *J of Chem Inf and Model* **62**, 1498-1509 (2022). https://doi.org/10.1021/acs.jcim.1c01304

65 Jo, S., Kim, T., Iyer, V. G. & Im, W. CHARMM-GUI: a web-based graphical user interface for CHARMM. *J Comput Chem* **29**, 1859-1865 (2008). https://doi.org/10.1002/jcc.20945

66 Tian, C. *et al.* ff19SB: Amino-acid-specific protein backbone parameters trained against quantum mechanics energy surfaces in solution. *J Chem Theory Comput* **16**, 528-552 (2020). https://doi.org/10.1021/acs.jctc.9b00591

67 Roe, D. R. & Cheatham, T. E., 3rd. PTRAJ and CPPTRAJ: Software for processing and analysis of molecular dynamics trajectory data. *J Chem Theory Comput* **9**, 3084-3095 (2013). https://doi.org/10.1021/ct400341p

68 Case, D. *et al.* AmberTools21. *University of California: San Francisco, CA, USA* (2021).

884 **Figure legends**

885 **Fig. 1. Adipo-*Zip13*KO mice exhibited accelerated lipolysis**

886 (A) Relative mRNA levels of *Zip13* in the indicated tissues of 34-week-old Ctrl (n = 5) and
887 Adipo-*Zip13*KO mice (n = 4). (B, C) Whole-body RER of 23-week-old Ctrl (n = 8) and Adipo-
888 *Zip13*KO mice (n = 9) fed a STD. (B) RER trend, (C) RER period. (D) Plasma NEFA levels of
889 22 to 27-weeek old Ctrl (n = 9) and Adipo-*Zip13*KO mice (n = 15) fasted overnight and the i.p.
890 injected with CL316,243. (E) NEFA release from the indicated mature adipocytes isolated from
891 subcutaneous and visceral fat tissues treated with dimethyl sulfoxide (DMSO) (Basal) or
892 isoproterenol (Iso). Mature adipocytes were obtained from 22- to 26-week-old Ctrl (n = 5) and
893 Adipo-*Zip13*KO mice (n = 5). NEFA release into the medium was normalized to the basal
894 control of the subcutaneous fat group. (F) NEFA release from Ctrl and Adipo-*Zip13*KO
895 differentiated cells treated with dimethyl sulfoxide (DMSO) (Basal) and isoproterenol (Iso).
896 Data are shown as the mean ± SEM. In (A, and C) $^{*}p < 0.05$, $^{**}p < 0.01$, $^{***}p < 0.001$, by the
897 two-tailed unpaired Student *t*-test. In (D, E, and F), $^{*}p < 0.05$, $^{**}p < 0.01$, $^{****}p < 0.0001$, by
898 two-way ANOVA followed by the Tukey's multiple comparison test for multiple group
899 comparisons. Circles indicate the data of individual mice. ns, not significant

900

901 **Fig. 2. Adipo-*Zip13*KO mice exhibited increased thermogenesis activity**

902 (A) Relative mRNA expression of *Zip13* in the subcutaneous fat tissue of WT mice (n = 5), fed
903 STD or HFD for 12 weeks from 6-weeks old. (B) Body weights of the indicted mice fed a STD

or HFD. Ctrl STD, n = 9 to 23; Adipo-*Zip13*KO STD, n = 7 to 19; Ctrl HFD, n = 17; Adipo-*Zip13*KO HFD, n = 22. (C) Body weight of 34-week-old Ctrl (n = 8) and Adipo-*Zip13*KO mice (n = 9). (D) Tissue weights of subcutaneous, visceral, and brown fat tissues of 34-week-old Ctrl (n = 8) and Adipo-*Zip13*KO (n = 9) mice. (E) Oxygen consumption rates of 21- to 31-week-old Ctrl (n = 9) and Adipo-*Zip13*KO (n = 7) mice treated with CL316,243 (0.5 mg/kg) under thermoneutral conditions. (A, B, C, and D) $^{*}p < 0.05$, $^{**}p < 0.01$, by the two-tailed unpaired Student *t*-test. In (E), $^{**}p < 0.01$, and $^{***}p < 0.001$, by two-way ANOVA followed by the Tukey's multiple comparison test for multiple group comparison. Circles indicate the data of individual mice. ns, not significant.

Fig. 3. Adipo-*Zip13*KO mouse adipocytes had increased intracytoplasmic iron levels but decreased organelle iron levels

(A) Iron (left) and zinc (right) levels in mature adipocytes, measured by ICP-MS. (B) Immunofluorescence staining of mZIP13-HA in preadipocytes. Insertion of an HA sequence at the C-terminal end enabled immunofluorescence studies to be performed using an anti-HA antibody. Scale bar: 50 μm. GM130, Golgi marker; calreticulin, ER marker. (C) Fe^{2+} (left) and Zn^{2+} (right) levels in Ctrl and Adipo-*Zip13*KO mature adipocyte cells. Fe^{2+} and Zn^{2+} levels were detected using FerroOrange and FluoZin-3, respectively. (D, E) Immunoblotting of IRP2, TfR, FTL, Fth1, aP2, and actin using whole cell extracts of differentiated Ctrl and Adipo-*Zip13*KO

cells treated with DMSO (Basal) (D) or isoproterenol (Iso) (E). Actin was included as a loading control. (F) Each protein shown in (D, E) was quantified by normalization to actin. Data are shown as the mean ± SEM. In (A, C and F), $^{*}p < 0.05$, $^{**}p < 0.01$, and $^{***}p < 0.001$, by the two-tailed unpaired Student *t*-test.

Fig. 4. PDE activity is reduced in Adipo-*Zip13*KO cells

(A) Schematic representation of the experimental plan (left panel). Ctrl and Adipo-*Zip13*KO cells were differentiated by stimulation with isoproterenol, in the presence or absence of N-acetylcysteine (NAC), and then NEFA release was analyzed (right panel). (B) Immunoblotting of pPKA, PKA, pCREB, CREB, pHSL, HSL, and GAPDH in subcutaneous fat tissues from 14 to 23-week-old Ctrl and Adipo-*Zip13*KO mice, in the basal condition (n = 4 mice each) (top left panels) or after treatment with isoproterenol (Iso) (n = 7 mice each) (top right panels). Phosphorylation levels in the upper panels were normalized by total protein (low bar graphs). (C) cAMP levels of Ctrl and Adipo-*Zip13*KO mature adipocytes in the presence (Iso) or absence (Basal) of isoproterenol. (D) NEFA release from differentiated Ctrl and Adipo-*Zip13*KO mature adipocytes stimulated with isoproterenol or forskolin. (E) PDE activity in Ctrl and Adipo-*Zip13*KO mature adipocytes, normalized by protein concentration. (F) PDE activity normalized by protein concentration of Ctrl adipocyte cells in the presence or absence of H_2O_2. Data are shown as the mean ± SEM. In (A, B, E, and F), $^{*}p < 0.05$, $^{**}p < 0.01$, $^{***}p < 0.001$, and $^{****}p < 0.0001$, by the two-tailed unpaired Student *t*-test. In (C and D), $^{*}p < 0.05$, and

943 ****$p < 0.0001$, by two-way ANOVA followed by the Tukey's multiple comparison test for
944 multiple group comparison. ns, not significant

945

946 **Fig. 5. ZIP13 has the ability to transport both Zn^{2+} and Fe^{2+}**

947 (A) Immunofluorescence microscopic detection of the expression of mZIP13, mZIP14, 4F2hc-
948 m13, and 4F2hc-m14 in *X. laevis* oocytes. Insertion of an HA sequence at the C-terminal end
949 enabled immunofluorescence analyses using an anti-HA antibody. Scale bars = 50 μm. (B)
950 Schematic illustration of 4F2hc-m13 and 4F2hc-m14. (C) Alphafold2 simulation of the fusion
951 protein of 4F2hc and mZIP13. (D) Relative *MT1* expression in HEK293 cells expressing 4F2hc,
952 4F2hc-m13, or 4F2hc-m14, without (Ctrl) or with the addition of 20 μM $ZnSO_4$ (Zn). (E) Zn^{2+}
953 uptake of 4F2hc, 4F2hc-m13, and 4F2hc-m14. (F) Fe^{2+} uptake of 4F2hc, 4F2hc-m13 and
954 4F2hc-m14. Data are shown as the mean ± SEM. In (E), ***$p < 0.001$, ****$p < 0.0001$, by one-
955 way ANOVA followed by the Tukey's multiple comparison test. In (D and F), **$p < 0.01$,
956 ****$p < 0.0001$, by the two-tailed unpaired Student *t*-test. Ext., extracellular space; Int.,
957 intracellular space

958

959 **Fig. 6. Ion-binding site prediction and analysis of the mouse ZIP13 protein**

960 (A) The ion-binding site within the representative structure of ZIP13 at M1 and M2, embedded
961 in the lipid membrane (right panel), and the motion of ions and amino acid residues in the M1

962 and M2 sites, where the red to blue color change indicates the time lapse (left panels). (B) The
963 number of atom contacts (#contacts) to ion during the 0.5-μs MD simulations. (C) Occupancy
964 of Zn^{2+}/Fe^{2+} ions within amino acid residues at the M1 and M2 sites. Oδ and Oε indicate two
965 different oxygens in the carboxy group, and Nε indicates the Nε atom in the histidine.
966
967 **Fig. 7. ZIP13 metal transport-incompetent mutant affects not only zinc but also iron**
968 **homeostasis**
969 (A) Schematic representation of the experimental plan. (B) Zn^{2+} (left) and Fe^{2+} (right) levels in
970 *Zip13*-KO preadipocytes expressing ZIP13-WT or ZIP13-H254A. (C) Zn^{2+} (left) and Fe^{2+}
971 (right) levels in *Zip13*-KO mature adipocytes expressing ZIP13-WT or ZIP13-H254A. (D)
972 Total iron levels of Ctrl and Adipo-*Zip13*KO preadipocytes and mature adipocytes. (E) Total
973 zinc levels of Ctrl and Adipo-*Zip13*KO preadipocytes and mature adipocytes. (F) Schematic
974 illustration of metal ion balance in preadipocytes and mature adipocytes. Total zinc levels
975 remain unchanged during adipocyte differentiation, whereas total iron levels substantially
976 increased during adipocyte differentiation. Data are shown as the mean ± SEM. In (B, and C),
977 $^{*}p < 0.05$, and $^{***}p < 0.001$, by one-way ANOVA followed by the Tukey's multiple comparison
978 test. In (D, and E), $^{**}p < 0.01$, by two-way ANOVA followed by the Tukey's multiple
979 comparison test for multiple group comparison. ns, not significant
980

Fig. 8. ZIP13 contributes to adipocyte lipolysis and thermogenesis through ZIP13-mediated iron

In control adipocytes (left panel), ZIP13-mediated iron homeostasis decreased cytosolic iron and suppresses the β-adrenergic receptor (AR) signaling pathway, thereby inhibiting lipolysis and thermogenesis. In Adipo-*Zip13*KO adipocytes (right panels), increased cytosolic iron downregulates PDE activity, thereby accelerated lipolysis and thermogenesis. Subcutaneous white adipose tissue releases NEFAs, which are utilized by brown adipose tissue as an energy source (lower right).

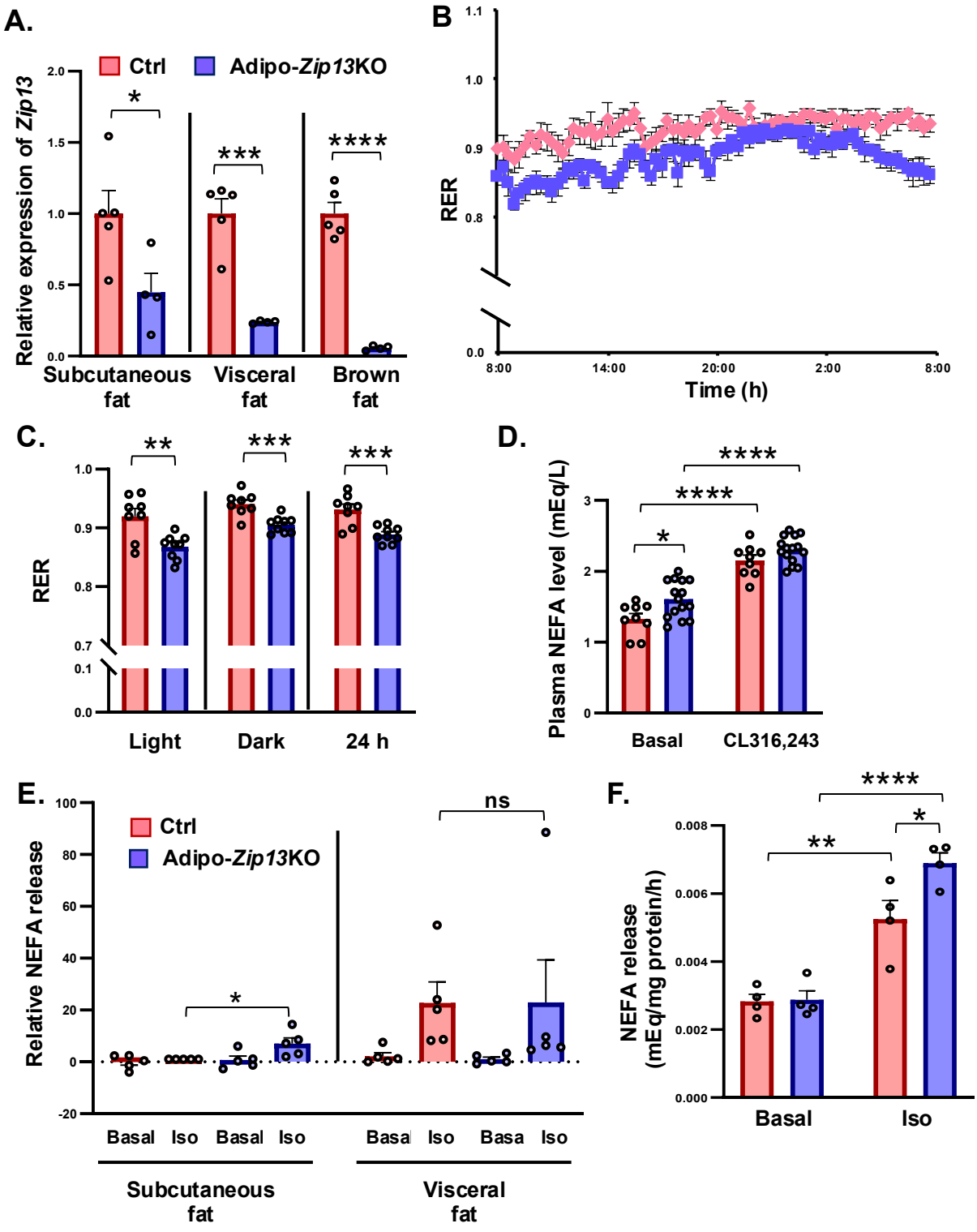

A.
Ctrl
Adipo-Zip13KO
Relative expression of Zip13
Subcutaneous fat
Visceral fat
Brown fat
B
RER
Time (h)
C.
RER
Light
Dark
24 h
D.
Plasma NEFA level (mEq/L)
Basal
CL316,243
E.
Relative NEFA release
Ctrl
Adipo-Zip13KO
ns
Basal
Iso
Subcutaneous fat
Visceral fat
F.
NEFA release (mEq/mg protein/h)
Basal
Iso

Fig. 1

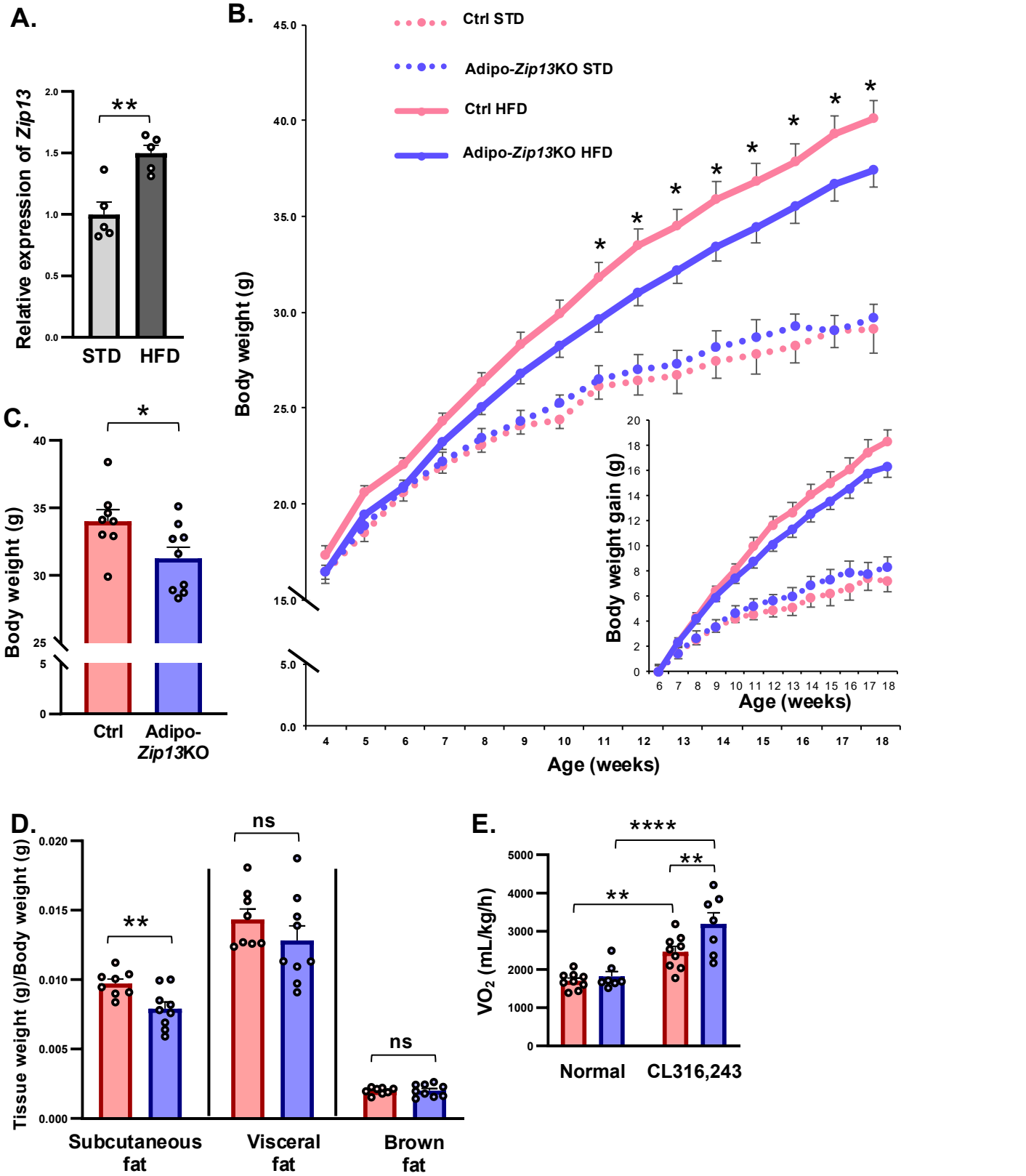

A.
Relative expression of Zip13
2.0
1.5
1.0
0.5
0.0
**
STD
HFD
B.
Ctrl STD
Adipo-Zip13KO STD
Ctrl HFD
Adipo-Zip13KO HFD
Body weight (g)
45.0
40.0
35.0
30.0
25.0
20.0
15.0
5.0
0.0
4
5
6
7
8
9
10
11
12
13
14
15
16
17
18
Age (weeks)
Body weight gain (g)
20
18
16
14
12
10
8
6
4
2
0
6
7
8
9
10
11
12
13
14
15
16
17
18
Age (weeks)
C.
Body weight (g)
40
35
30
25
5
0
*
Ctrl
Adipo-Zip13KO
D.
Tissue weight (g)/Body weight (g)
0.020
0.015
0.010
0.005
0.000
**
ns
ns
Subcutaneous fat
Visceral fat
Brown fat
E.
VO2 (mL/kg/h)
5000
4000
3000
2000
1000
0
****
**
**
Normal
CL316,243

Fig. 2

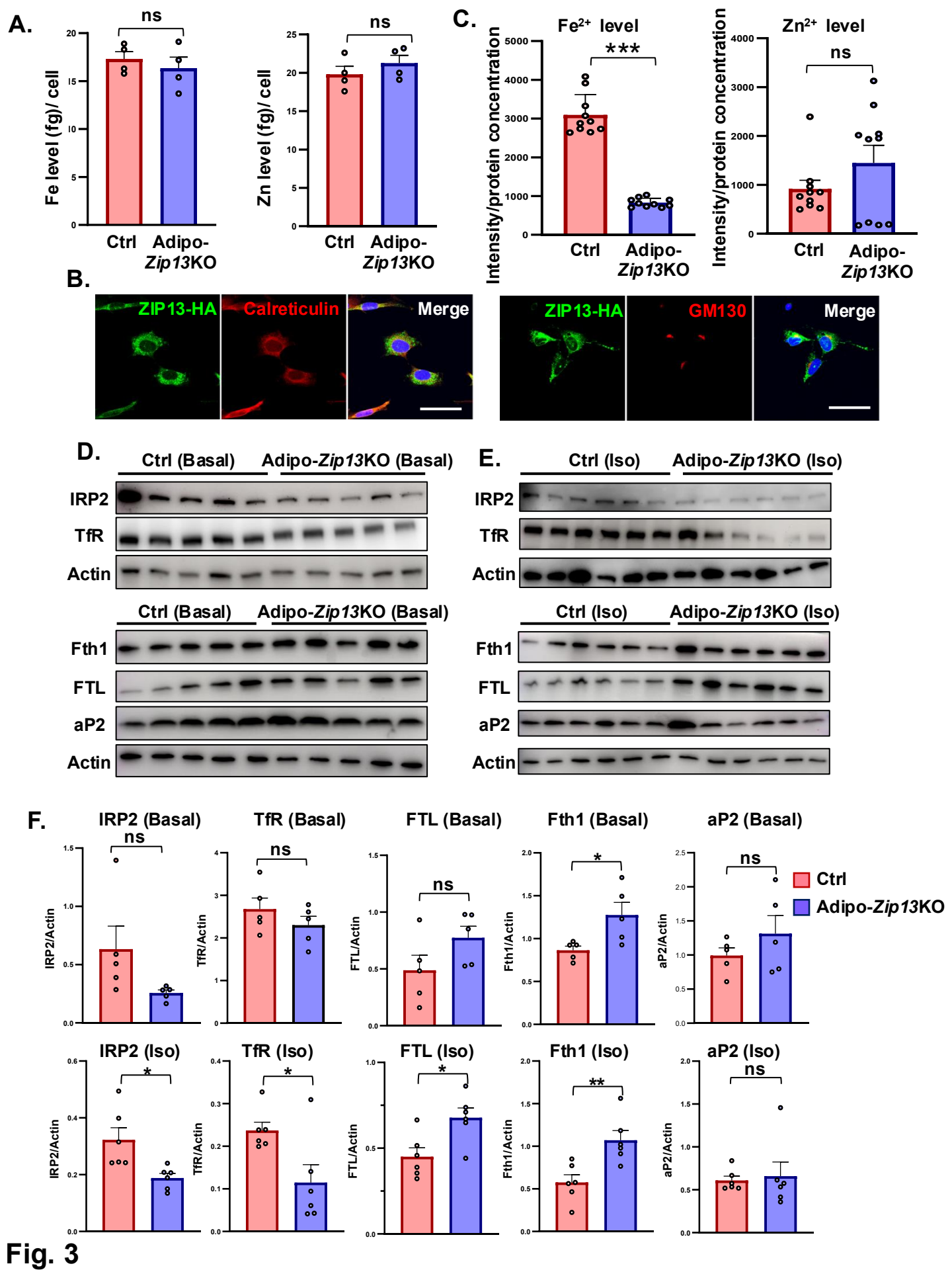

A.
ns
Fe level (fg)/ cell
Ctrl
Adipo-Zip13KO
ns
Zn level (fg)/ cell
Ctrl
Adipo-Zip13KO
C.
Fe2+ level
***
Intensity/protein concentration
Ctrl
Adipo-Zip13KO
Zn2+ level
ns
Intensity/protein concentration
Ctrl
Adipo-Zip13KO
B.
ZIP13-HA
Calreticulin
Merge
ZIP13-HA
GM130
Merge
D.
Ctrl (Basal)
Adipo-Zip13KO (Basal)
IRP2
TfR
Actin
Ctrl (Basal)
Adipo-Zip13KO (Basal)
Fth1
FTL
aP2
Actin
E.
Ctrl (Iso)
Adipo-Zip13KO (Iso)
IRP2
TfR
Actin
Ctrl (Iso)
Adipo-Zip13KO (Iso)
Fth1
FTL
aP2
Actin
F.
IRP2 (Basal)
ns
IRP2/Actin
TfR (Basal)
ns
TfR/Actin
FTL (Basal)
ns
FTL/Actin
Fth1 (Basal)
*
Fth1/Actin
aP2 (Basal)
ns
aP2/Actin
Ctrl
Adipo-Zip13KO
IRP2 (Iso)
*
IRP2/Actin
TfR (Iso)
*
TfR/Actin
FTL (Iso)
*
FTL/Actin
Fth1 (Iso)
**
Fth1/Actin
aP2 (Iso)
ns
aP2/Actin

Fig. 3

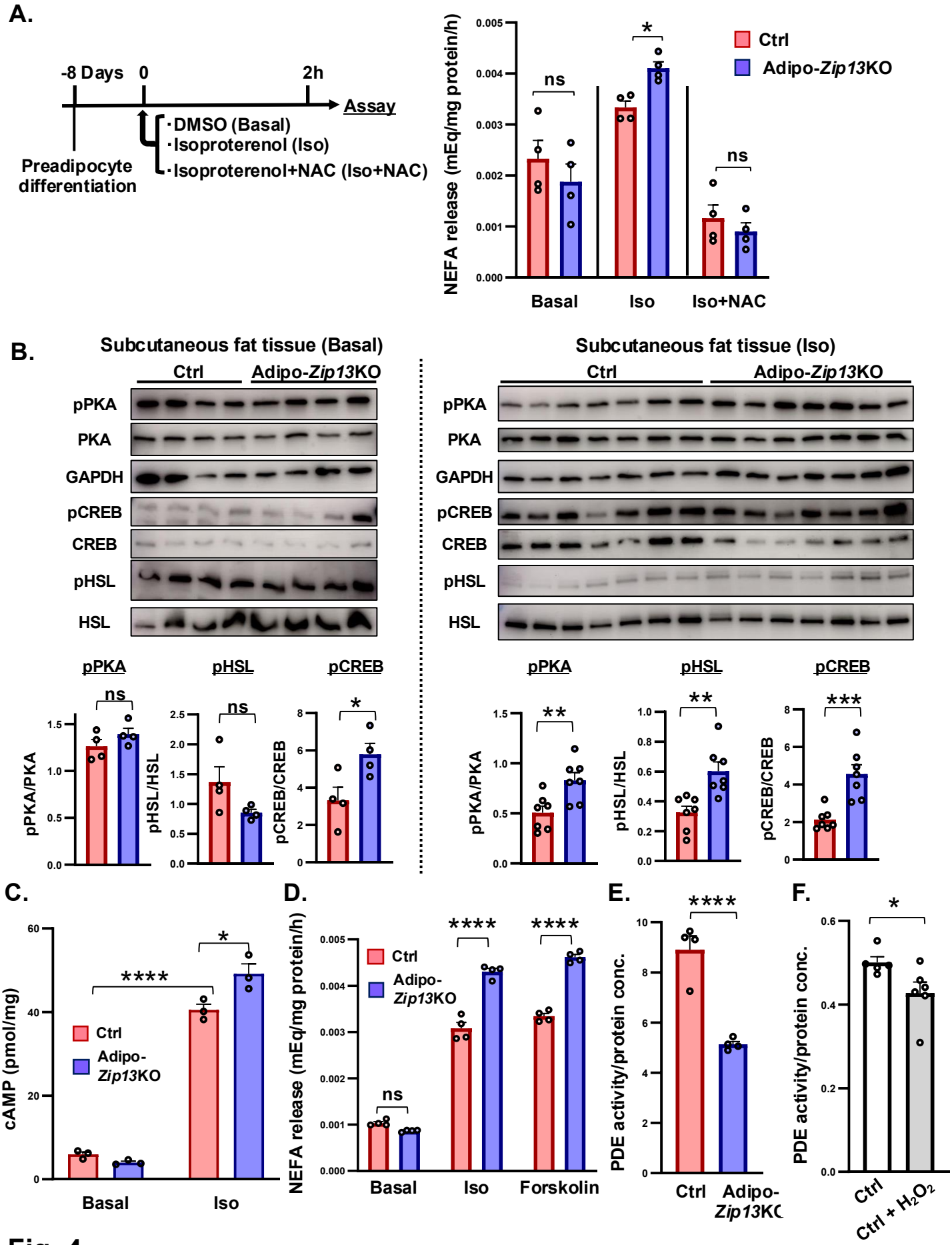

A.
-8 Days
0
2h
Assay
·DMSO (Basal)
·Isoproterenol (Iso)
·Isoproterenol+NAC (Iso+NAC)
Preadipocyte differentiation
NEFA release (mEq/mg protein/h)
Ctrl
Adipo-Zip13KO
ns
*
ns
Basal
Iso
Iso+NAC
B.
Subcutaneous fat tissue (Basal)
Subcutaneous fat tissue (Iso)
Ctrl
Adipo-Zip13KO
pPKA
PKA
GAPDH
pCREB
CREB
pHSL
HSL
pPKA
pHSL
pCREB
pPKA/PKA
pHSL/HSL
pCREB/CREB
ns
ns
*
**
**
***
C.
cAMP (pmol/mg)
Ctrl
Adipo-Zip13KO
****
*
Basal
Iso
D.
NEFA release (mEq/mg protein/h)
Ctrl
Adipo-Zip13KO
ns
****
****
Basal
Iso
Forskolin
E.
PDE activity/protein conc.
****
Ctrl
Adipo-Zip13KO
F.
PDE activity/protein conc.
*
Ctrl
Ctrl + H2O2

Fig. 4

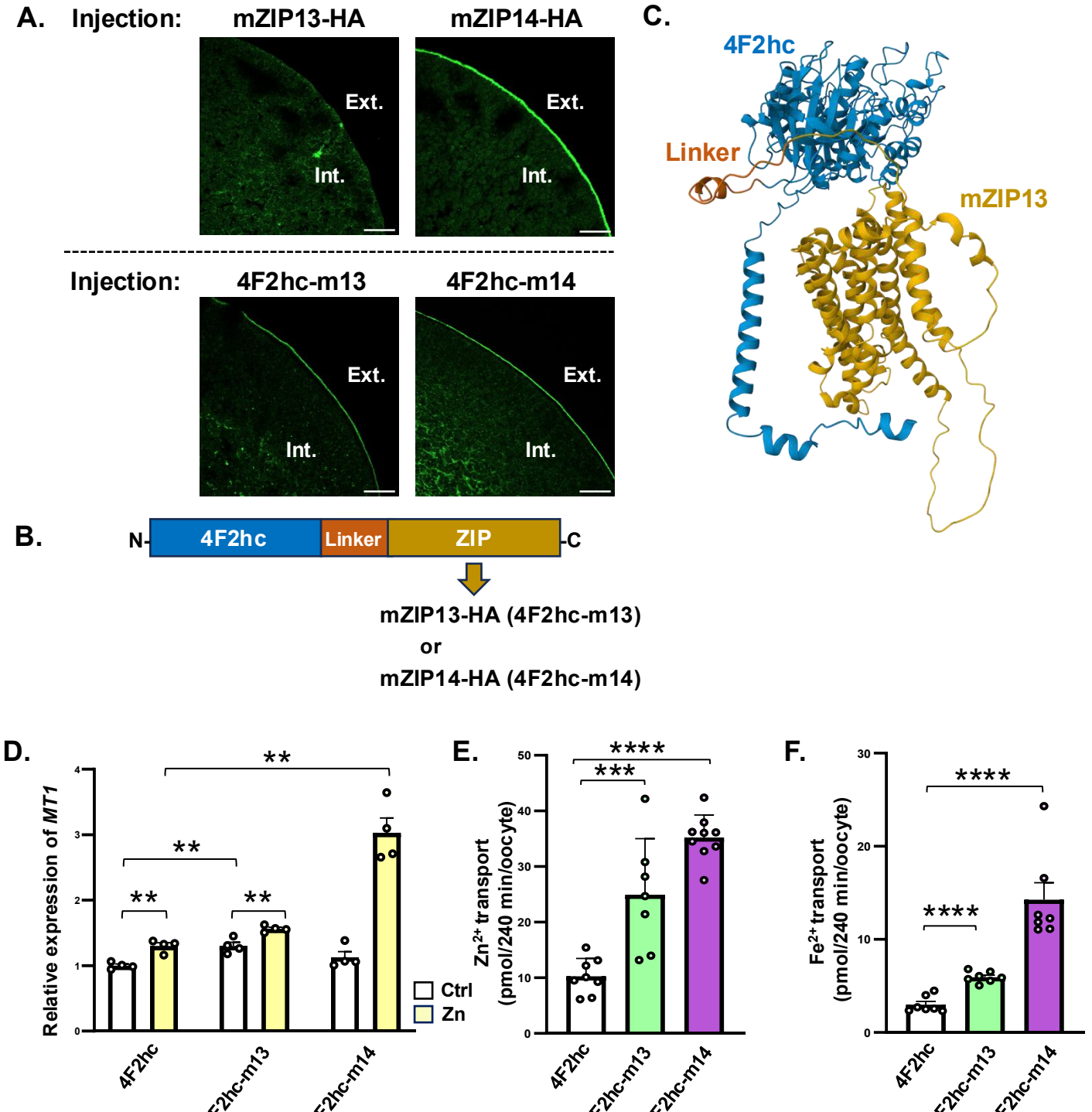

A.
Injection:
mZIP13-HA
mZIP14-HA
Ext.
Int.
Injection:
4F2hc-m13
4F2hc-m14
C.
4F2hc
Linker
mZIP13
B.
N-
4F2hc
Linker
ZIP
-C
mZIP13-HA (4F2hc-m13)
or
mZIP14-HA (4F2hc-m14)
D.
Relative expression of MT1
Ctrl
Zn
4F2hc
4F2hc-m13
4F2hc-m14
E.
Zn2+ transport
(pmol/240 min/oocyte)
F.
Fe2+ transport
(pmol/240 min/oocyte)

Fig. 5

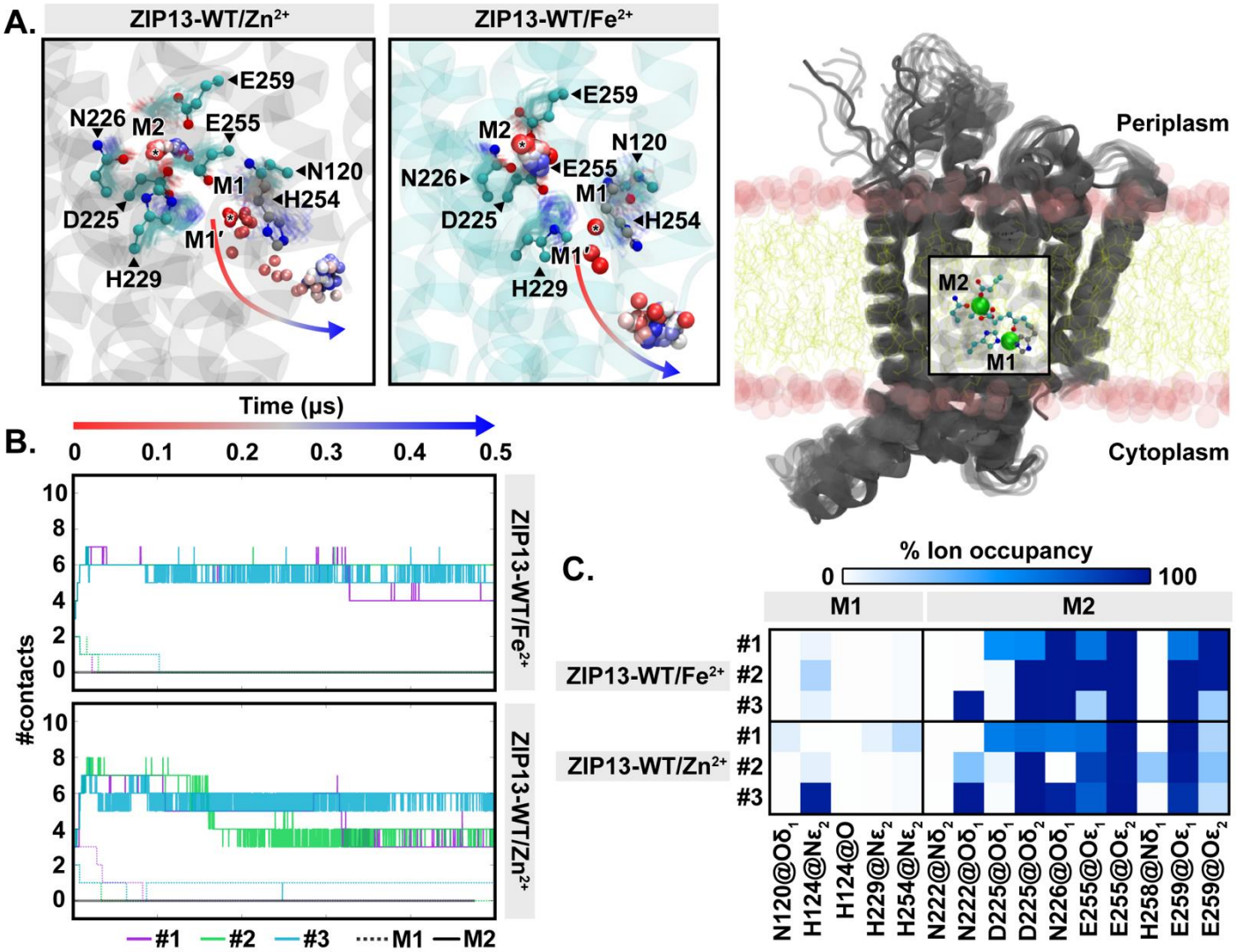

A.
ZIP13-WT/Zn2+
ZIP13-WT/Fe2+
E259
N226
M2
E255
N120
M1
H254
D225
M1'
H229
Periplasm
Cytoplasm
B.
Time (μs)
0
0.1
0.2
0.3
0.4
0.5
#contacts
ZIP13-WT/Fe2+
ZIP13-WT/Zn2+
#1
#2
#3
M1
M2
C.
% Ion occupancy
0
100
M1
M2
ZIP13-WT/Fe2+
ZIP13-WT/Zn2+
N120@Oδ1
H124@Nε2
H124@O
H229@Nε2
H254@Nε2
N222@Nδ2
N222@Oδ1
D225@Oδ1
D225@Oδ2
N226@Oδ1
E255@Oε1
E255@Oε2
H258@Nδ1
E259@Oε1
E259@Oε2

Fig. 6

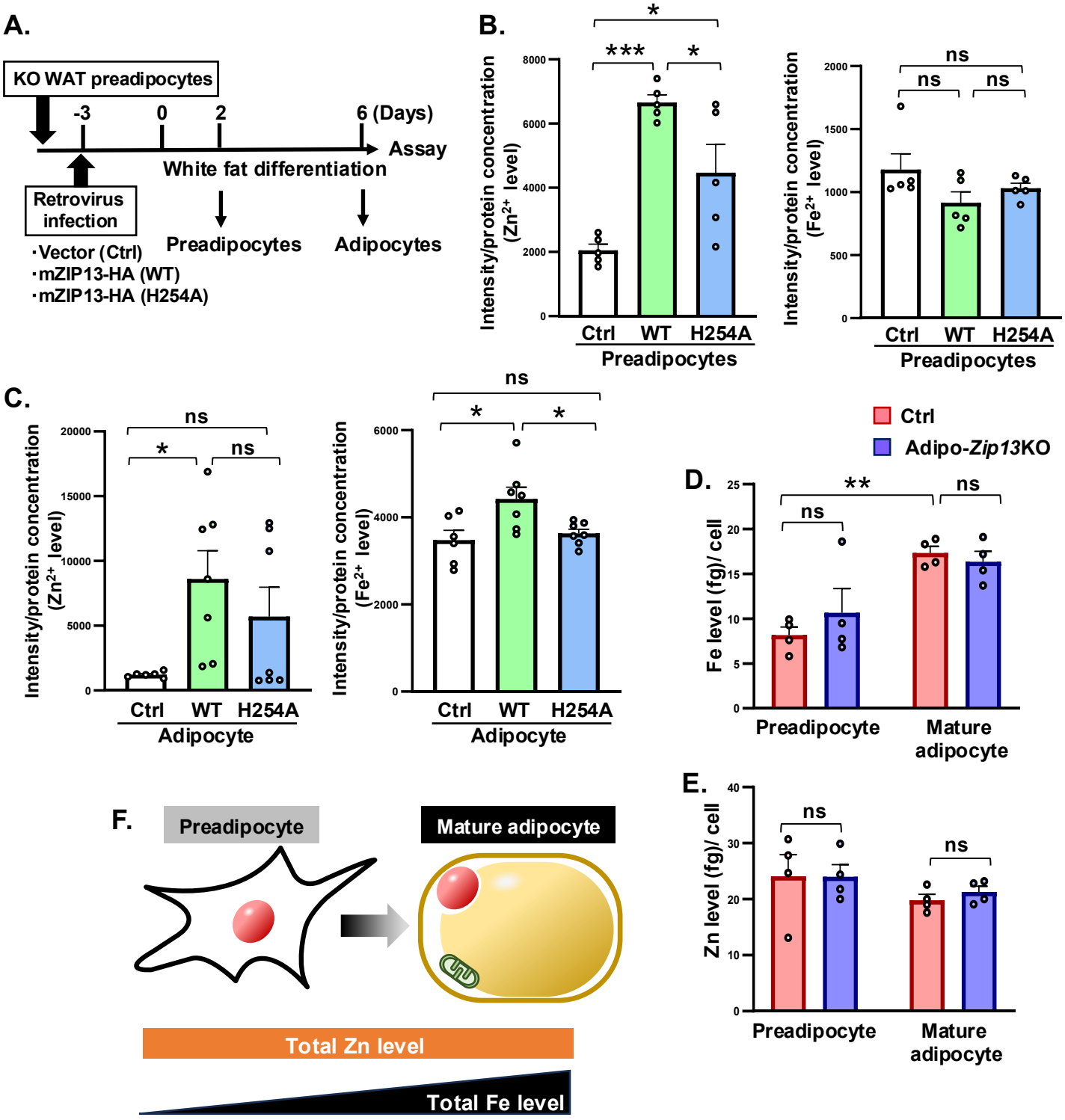

A.
KO WAT preadipocytes
-3
0
2
6 (Days)
Assay
White fat differentiation
Retrovirus infection
Preadipocytes
Adipocytes
·Vector (Ctrl)
·mZIP13-HA (WT)
·mZIP13-HA (H254A)
B.
Intensity/protein concentration (Zn2+ level)
Ctrl
WT
H254A
Preadipocytes
Intensity/protein concentration (Fe2+ level)
ns
C.
Intensity/protein concentration (Zn2+ level)
Adipocyte
Intensity/protein concentration (Fe2+ level)
Ctrl
Adipo-Zip13KO
D.
Fe level (fg)/ cell
Preadipocyte
Mature adipocyte
E.
Zn level (fg)/ cell
F.
Preadipocyte
Mature adipocyte
Total Zn level
Total Fe level

Fig. 7

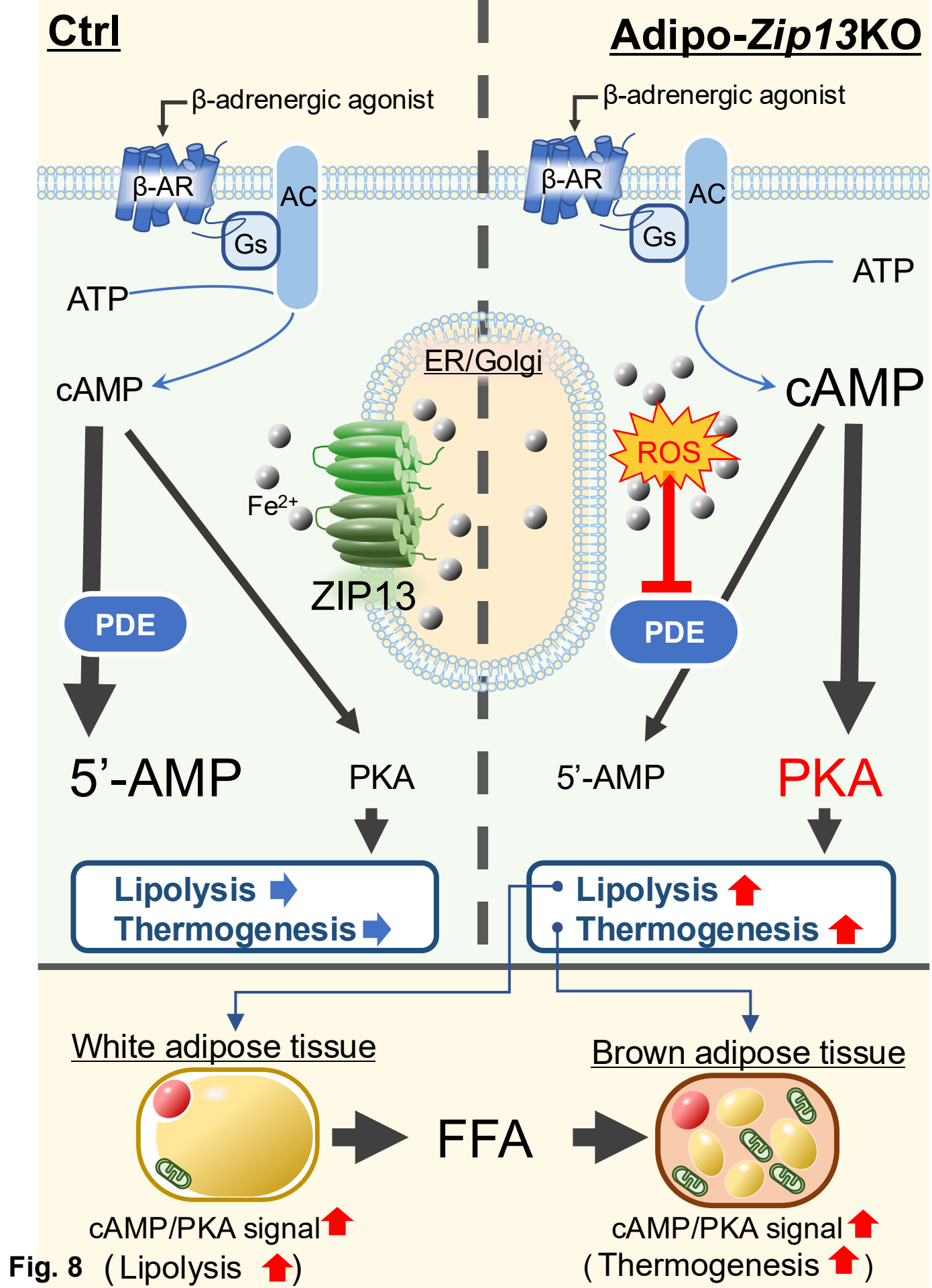

Ctrl
Adipo-Zip13KO
β-adrenergic agonist
β-AR
AC
Gs
ATP
cAMP
ER/Golgi
Fe2+
ZIP13
ROS
PDE
5'-AMP
PKA
Lipolysis
Thermogenesis
White adipose tissue
Brown adipose tissue
FFA
cAMP/PKA signal
(Lipolysis)
(Thermogenesis)

Fig. 8

Supplementary Files

This is a list of supplementary files associated with this preprint. Click to download.

- FinalSupplementalFiguresourcedata.xlsx
- Supplementalfile.pdf
- Finalsourcedata.xlsx